Impact Loading of Timber Beams

by

Bengt Jansson

M.Sc.(Civ.Eng.), Lund Institute of Technology, Lund, Sweden, 1987.

A THESIS SUBMITTED IN PARTIAL FULFILLMENT OF

THE REQUIREMENTS FOR THE DEGREE OF

MASTER OF APPLIED SCIENCE

in

THE FACULTY OF GRADUATE STUDIES

DEPARTMENT OF CIVIL ENGINEERING

We accept this thesis as conforming

to the required standard

THE UNIVERSITY OF BRITISH COLUMBIA

April 1992

In presenting this thesis in partial fulfilment of the requirements for an advanced degree at the University of British Columbia, I agree that the Library shall make it freely available for reference and study. I further agree that permission for extensive copying of this thesis for scholarly purposes may be granted by the head of my department or by his or her representatives. It is understood that copying or publication of this thesis for financial gain shall not be allowed without my written permission.

(Signatur

Department of CIVIL ENGINEERING

The University of British Columbia
Vancouver, Canada

Date APRIL 30th 1992

DE-6 (2/88)

Abstract

Static tests as well as impact tests were performed to build up our knowledge about impact loading of timber beams. The investigation was focused on failure modes and failure stresses. The static tests were conducted using both deformation and load controlled regimes at three different loading rates in a MTS test machine. The single blow impact tests were carried out with three different drop-heights using a drop-weight impact machine built at the University of British Columbia.

A total of 651 specimens (38 x 89 x 1145 mm) were sorted into two categories. The specimens were then grouped into the various loading groups according to the modulus of elasticity obtained from non-destructive bending tests.

Three different dynamic failure stress analyses were applied and compared with each other. The distributed inertial forces were replaced with a mid-point inertial force in the first analysis, which was based upon accelerometer measurements. The accelerometer measurements from these tests were considered very unreliable. The second analysis employed a very detailed finite element program which went beyond the objectives of this thesis. The third analysis was a modal analysis, which was a mode-superposition analysis of a distributed-parameter system. The modal analysis was used throughout the remaining analysis because its solution was easily divided into its static and dynamic parts, and it was more efficient than the second analysis.

The strength ratio, which was the ratio between dynamic and static failure stress, reflected the effect of impact loading better than the traditional duration of load theory.

Non-parametric percentile values of the strength ratio based on the distribution

of strength ratios were found more appropriate than if these percentile values were based on the distribution of failure stresses.

No differences in failure stresses were observed between the different static tests. A strength decrease of 15 % was experienced for the weaker specimen.

The overall tendency was that the number of compression initiated failures decreased with decreasing failure time. The decrease in failure strength with decreasing failure time was explained by the decreasing amount of compression initiated failure modes.

Table of Contents

List of Figures

List of Tables

Acknowledgement

The author is very grateful to his supervisor Professor Borg Madsen for his guidance, valuable suggestions, and encouragement throughout this research.

The author express his gratitude to Professor R.O. Foschi for theoretical guidance and for reviewing the manuscript, and Professor S. Mindess for reviewing the manuscript and making constructive criticism.

Appreciation is extended to Mr. C.Y. Cheng, Mr. A. Chu, Mr. M. Nazar, Mr. P. Symons, and Mr. W. Yung for the helpful participation in preparing and maintaining instrumentation used in the experimental part of this research, and for necessarry assistance during the various investigations.

Research grants and other financial support from various societies and institutes in Sweden and Canada are gratefully acknowledged.

The author wish to thank his family and friends for their support throughout his graduate career.

Chapter 1

Introduction

1.1 Background

The character of impact loading is very different than that of static loading and it is important to understand this difference. Figure 1.1 shows schematically how impact loads relate to static, vibration, wind, earthquake and blast loads in terms of loading time or duration of load.

Impact loading defined as single blow impact occurs in quite a few cases, i.e.:

- accidental fall of weights on structures,
- ferries docking in harbours,
- tornado missiles (i.e. pieces of lost structures),
- highway railings,
- railway ties,
- pile driving.

The impacting mass and velocity are very different in each of these applications, as well as the mass, damping and stiffness properties of the structure subjected to the impact.

According to tradition a timber beam is expected to resist higher stresses during impact loading than during static loading. The worldwide practice in timber design codes is to double the 10-year longterm strength to get the strength at impact load. In the Engineering Design in Wood (Limit States Design) from 1989 (Canadian Standard Association, 1989) the design stress is 15 % higher for short term duration loading compared to standard term loading. Short term loading means that condition of

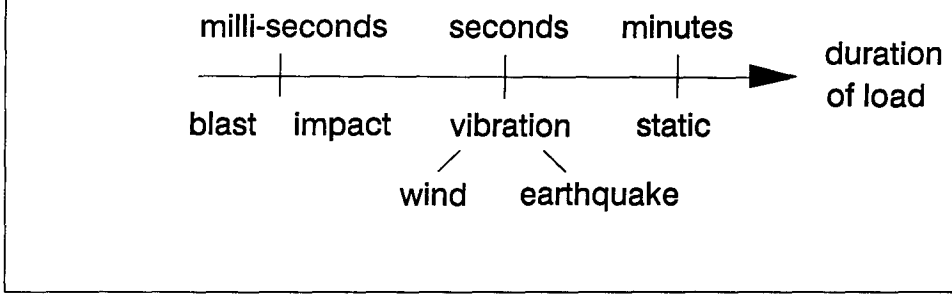

Figure 1.1: Duration of various loads.

loading where the duration of a specific load is not expected to last more than 7 days continuously or cumulatively throughout the life of the structure. Examples of short term loading include wind loads, earthquake loads, falsework, and formwork as well as impact loads. Standard term means a condition of loading where the duration of specified loads exceeds that of short term loading, but is less than permanent loading. It should be noticed that standard term loading includes snow loads, live loads due to occupacy, wheel loads on bridges, and dead loads in combination with all of the above provided taht the dead load is less than 50 % of the total load.

It is important to have a good understanding of the character of impact loads and to realize the clear distinction between impact loads and other short term loads.

1.2 Literature Review

1.2.1 Introduction

This section gives a brief summary of earlier impact tests, fast rate of loading tests, and more recent impact tests at the University of British Columbia (UBC). Some of these tests were performed on small clear wood beams, and others were carried

out on wood and timber beams. Small clear wood beams were small beams of clear defect-free wood. Wood beams were beams of as 'clear' as possible wood material. Timber beams were beams of commercially available lumber.

1.2.2 Early Impact Tests

Impact testing of wood dates back to the beginning of our century, when the applications were wagon wheels, hammer handles, airplanes, and baseball bats. Different impact bending machines were developed and tested against each other. The influence of shape and size of beams, notches, grain angle, density, moisture content, temperature, anatomical properties, chemical constituents, and decay on the impact strength was extensively investigated for small clear specimen of wood. The impact test procedures can be divided into single blow and successive blow impact tests. The most commonly used testing machines were of drop-weight type (the French guillotine) or pendulum type (the Charpy test). Various researchers (Wilson, 1922; Drow et al., 1958; and Kollmann and Côté, 1968) have reported on these early impact tests on small clear specimen of wood.

1.2.3 Fast Rate of Loading Tests

Rapid loading tests (Liska, 1950) and a single data point from impact tests (Elmendorf, 1916) with a failure time of 0.013 sec., contributed to the development of the load duration curve (Wood, 1951), also called the 'Madison-curve'.

The long term loading effects on the strength of timber beams are very well documented and were found not to comply with the 'Madison-curve' by various researchers (Madsen, 1971; Spencer, 1978). Less work has been carried out in the area of fast rate of loading of timber beams.

Commercially available lumber was tested at eight different rates of stressing

(Spencer, 1978). The ramp loading was applied at constant rates of loading. Four-point bending was performed on 38 mm wide, 140 mm deep and 3660 mm long boards of Douglas-fir at a clear span of 2515 mm. The stronger boards showed an increasing strength as the rate of stressing increased. The weaker boards showed no change in strength as the rate of stressing increased. At the higher rate of stressing a significantly higher proportion of splinting tension failure, which resulted in boards breaking into completely separate pieces, was observed. The highest rate of loading gave an average failure time of 0.061 sec.

1.2.4 More Recent Impact Tests at UBC

More recent impact tests on wood and timber beams were performed in an instrumented drop-weight impact machine designed by Professor S. Mindess and built in the Structural Laboratory at the Department of Civil Engineering, University of British Columbia (UBC). The impact machine was capable of dropping a 345 kg mass impact hammer from heights of up to 3 m.

Three different specimens: clear wood, clear wood with a notch at the bottom of the specimen, and wood with a large knot located near the bottom face were tested and photographic records of crack patterns were presented (Mindess and Madsen, 1986). The beams (38 x 134 x 914 mm) were tested in a clear span of 610 mm. Photographs were taken with a high speed motion camera at a rate of 500 frames per second, which permitted the crack development during the fracture event to be monitored. The behaviour of wood under impact loading appeared to be physically different from its behaviour under static loading. The behaviour of all three specimens was similar. After some initial crushing at the point of impact, failure occurred by the propagation of a single crack from the bottom face of the beam to the point of impact with tensile failure of the longitudinal fibres. The size of the striking head of

the impact machine must have played a significant role in the initial crushing of the wood fibres.

In another test, large commercial timber beams (102 x 203 x 1530 mm) were tested on a clear span of 1219 mm at three different drop heights (1.5 m, 1.75 m, and 2.0 m) and their responses were compared to a control group tested under static loading, where failure occured in about 1 minute (Mindess et al., 1988). It appeared that, under impact loading, both the peak bending loads and fracture energies were lower than those obtained under static loading. Differences in failure modes were also observed between impact and static loading. In the static tests extensive longitudinal crack propagation always preceded failure, while in impact tests a single jagged vertical crack from the bottom of the beam to the point of impact caused the failure. A considerable indentation was also created in these tests by the impacting hammer into the beam specimen, before any crack propagation was observed, caused by the impacting bending load.

1.3 Objective and Scope

The aim of this thesis is to:

- study the behaviour of timber beams under single blow impact, and
- to understand and quantify the differences between static and impact loading.

To understand and quantify the differences between static and impact loading, both static and impact tests had to be performed. Different failure characteristics, such as the failure stress, the failure time and the failure mode, had to be monitored. The simply supported beam loaded at the mid-point was chosen as the structural member to be studied under impact loading, because it is both a practically and theoretically well documented case.

More specifically in this thesis:

- the indentation or crushing problems observed in earlier impact tests at UBC had to be eliminated,
- theoretical studies had to be performed to find out how different assumptions effect the impact failure bending stress calculated by different failure stress analyses,
- various analyses had to be applied and compared to each other,
- investigations had to be carried out as to whether or not the failure modes were different in impact loading as compared to static loading, and
- analysis had to performed to determined whether the impact strength increases, decreases or remains unchanged as compared to the static strength for timber.

Chapter 2

Theoretical Considerations

2.1 Introduction

This chapter presents the three different theories used when analysing the data from the static and impact bending tests. The dynamic analysis itself was approached with three different analyses.

- Static Analysis (section 2.2).
- Stress Wave Analysis (section 2.3).
- Dynamic Analysis (section 2.4):
  - Earlier Analysis (section 2.4.9).
  - FENTAB Analysis (section 2.4.10).
  - Modal Analysis (section 2.4.11).

The impact bending tests fell in the area of dynamic analysis because the striking velocity was expected to be significant but less then 250 m/sec. Below this velocity level the characteristics are local indentation or penetration, which are strongly coupled to the overall deformation of the structure. For impact loading the loading and response times are in the milli-second regime (Zukas et al., 1982).

The effect of the time-history of loading is considered in dynamic analysis. Dynamic analysis seemed to be the best approach because it can satisfy the desire to

study the behaviour of impact loading, and to understand and quantify the differences between static and impact loading.

Both the static analysis and the basic stress wave analysis are presented in the next two sections. The static analysis was used both for comparative purposes and for computing the modulus of elasticity. The stress wave analysis was employed to assure that the applied load could be considered to be transferred into stresses instantaneously all over the beam.

An introduction is given to some of the general terms and concepts that are common for the various dynamic analyses. The various dynamic analyses are presented before some basic terms are given for the statistical analysis. The chapter ends with a discussion of some concepts in the field of impulsive load response.

2.2 Static Analysis

If a beam is assumed to have a linear elastic behaviour, a constant cross section, is simply supported, and is loaded statically in the midspan, then the maximum bending stress f_{max} and the modulus of elasticity E can be calculated as follows.

$$f_{max} = \frac{M_{max}}{S} = \frac{P_{max}L}{4S} \quad \text{and} \quad E = \left(\frac{P}{\Delta}\right)\frac{L^3}{48I} \tag{2.1}$$

In the expressions above M_{max} is the maximum bending moment, S is the section modulus, P_{max} is the maximum applied force, L is the clear span between the supports, P/Δ is the slope of the load-deflection curve, and I is the moment of inertia. For a rectangular cross section the section modulus and moment of inertia are

$$S = \frac{bd^2}{6} \quad \text{and} \quad I = \frac{bd^3}{12} \tag{2.2}$$

respectively, where b is the width and d is the depth of the beam. Figure 2.1 shows the configuration of a static bending test where P is the concentrated midspan load and Δ is the corresponding deflection.

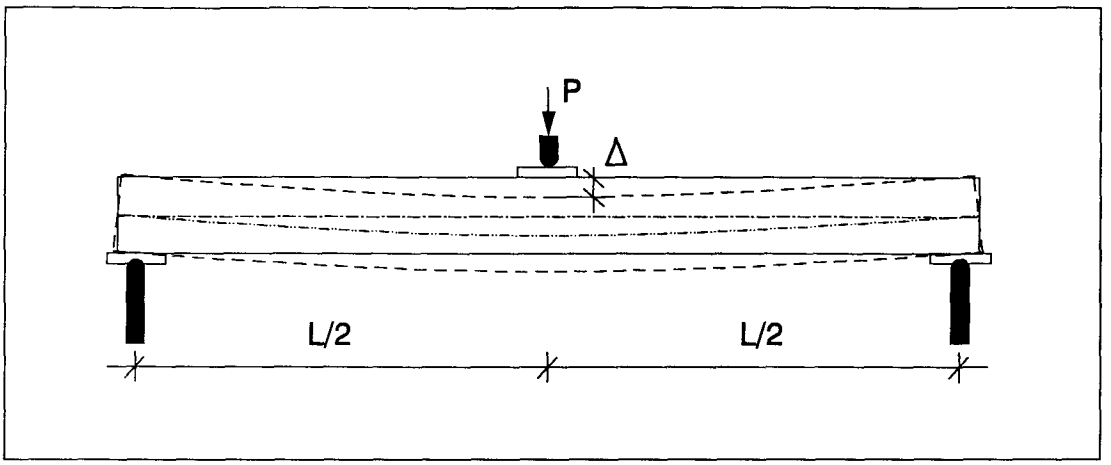

Figure 2.1: Mid-point loaded simply supported beam.

2.3 Stress Wave Analysis

When a force is applied to a body a stress wave is initiated at the point and time, of application of the force. This stress wave travels through the body (Harris, 1959). Elastic theory of isotropic solids indicates two types of stress waves. Dilatational waves, also called longitudinal or compression waves, are those in which the particle motions are induced by disturbances normal to the wave front. Distortional waves, also called transverse or shear waves, are those wherein material particles move perpendicular to the wave front. Expressions for the velocity of propagation in material for longitudinal and shear waves, denoted by c_L and c_S, and are defined as follows:

$$c_L = \sqrt{\frac{E}{\rho}} \quad \text{and} \quad c_S = \sqrt{\frac{G}{\rho}} \tag{2.3}$$

respectively, where E is the modulus of elasticity, G is the shear modulus and ρ is the density of the material (Zukas et al., 1982).

The longitudinal wave propagation velocity c_L provides an indication of how long it took for the applied stress to travel throughout the beam.

2.4 Dynamic Analysis

Three different approaches to a dynamic failure stress analysis are presented and compared in this section, and they are as follows.

- Earlier Analysis (section 2.4.9).
- FENTAB Analysis (section 2.4.10).
- Modal Analysis (section 2.4.11).

The analysis used in earlier drop-weight impact tests at UBC, as presented in section 1.2.4, are defined as the earlier analysis in this thesis. The earlier analysis was based on a generalized inertial load assumption. The FENTAB analysis was used in studies of beams under air-blast pressure pulses and was performed with a finite element program. The modal analysis was a mode-superposition analysis of the dynamic response of a distributed-parameter system.

The fundamental characteristics of a dynamic problem are given together with some of the basic concepts of dynamic analysis as a general introduction to this section on dynamic analysis. These basic concepts are later used in the three dynamic analyses that are presented at the end of this section.

2.4.1 Fundamental Characteristics of a Dynamic Problem

The fundamental distinction between static and dynamic problems is illustrated in Figure 2.2 for a simple beam subjected to a midspan load P. The internal moments, internal shears and deflected shape of the static loaded beam in Figure 2.2(a) depend directly upon the given load and can be computed by established principles of force equilibrium. If the load $P(t)$ is applied dynamically, as shown in Figure 2.2(b), the resulting displacements of the beam are associated with accelerations which produce

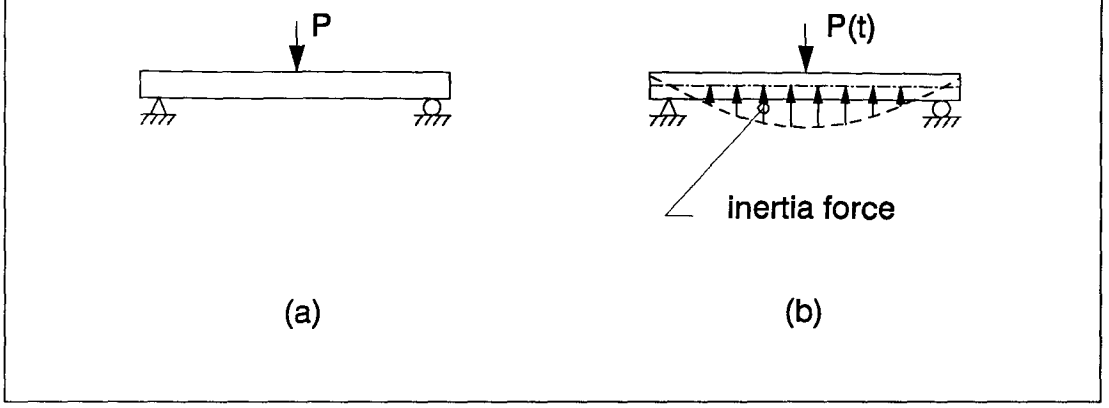

Figure 2.2: Basic difference between (a) static and (b) dynamic loading.

inertia forces resisting the accelerations. Thus the internal moments and internal shears in the dynamic loaded beam must equilibrate not only the externally applied force but also the inertia forces resulting from the accelerations of the beam (Clough and Penzien, 1985).

2.4.2 Single-Degree-of-Freedom System

The essential physical properties of any linearly elastic structural system subjected to dynamic loads include its mass, its elastic properties (flexibility or stiffness), its energy-loss mechanism or damping, and the external source of excitation or loading. In the simplest model of a single-degree-of-freedom (SDOF) system, each of these properties is assumed to be concentrated in a single physical element. A sketch of such a idealized SDOF system is shown in Figure 2.3.

The basic equation of motion for a SDOF system or a simple spring-mass system with damping, is

$$m\ddot{y}(t) + c\dot{y}(t) + ky(t) = p(t), \tag{2.4}$$

where m is the mass, c is the damping and k is the stiffness. The general displacement

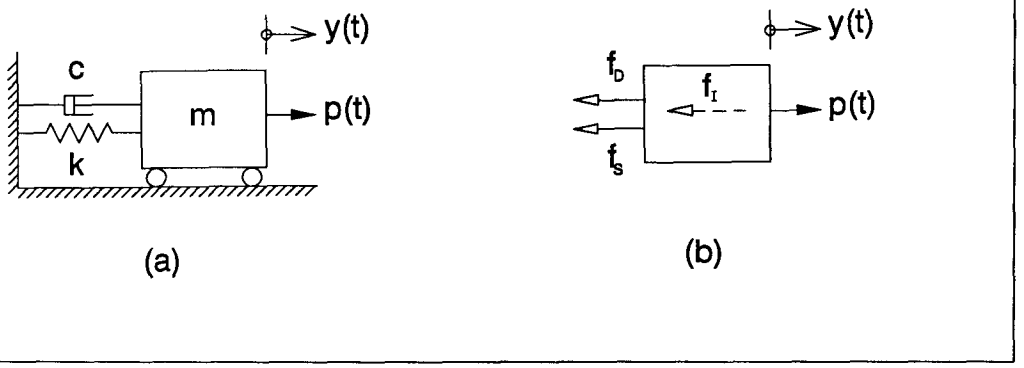

Figure 2.3: Idealized SDOF: (a) basic components, (b) forces in equilibrium.

solution of the SDOF system $y(t)$ can be obtained by dividing the equation up to a homogeneous equation $y_h(t)$ and a particular equation $y_p(t)$, as

$$y(t) = y_h(t) + y_p(t). \tag{2.5}$$

In the homogeneous solution the motion taking place is applied with the force set equal to zero and is called free vibration. The particular solution is the specific behaviour generated by the form of the applied dynamic load and creates steady-state vibration. It should be noted that the results from the SDOF system also apply to a generalized-coordinate system of any complex system which can been reduced to a SDOF system.

The free-vibration response of the underdamped SDOF system is given as

$$y_h(t) = e^{-\xi\omega t}\left(A\sin\omega_d t + B\cos\omega_d t\right), \tag{2.6}$$

in which A and B are constants, and

$$\omega_d = \omega\sqrt{1-\xi^2} \quad \text{and} \quad \omega = \sqrt{\frac{k}{m}} = 2\pi f = \frac{2\pi}{T}. \tag{2.7}$$

The quantity ω is the circular frequency or angular velocity of the motion and is measured in radians per unit time. The subscript d refers to the damped frequency.

The cyclic frequency f is usually referred to as the frequency of motion and its recipical is called the period T. The damping ratio or the damping factor ξ is defined as,

$$\xi = \frac{c}{c_c} = \frac{c}{2m\omega}, \tag{2.8}$$

where c_c is the critical damping value. If the damping is less than the critical damping value the system is underdamped.

For low values of the damping ratio ξ can be calculated with sufficient accuracy by using

$$\xi \doteq \frac{y_n - y_{n+1}}{2\pi y_{n+1}}, \tag{2.9}$$

where '$\doteq$' represents 'approximately equal', y_n is the nth positive peak displacement and y_{n+1} is the successive positive peak displacement.

In typical structural systems the damping ratio is usually less than 20 % and consequently the damped vibration frequency differs very little from the undamped frequency. From some damping tests performed in this investigation, which are presented in section 4.6, the damping ratio was found to be 3-5% for the given specimen.

2.4.3 Generalized SDOF System

If the motion of a system can be described by a single coordinate and no other motion is possible then the system is a SDOF system. The solution of the basic equation of motion for a SDOF system is then the exact dynamic response. But if the structure actually has more than one possible mode of displacement and if the structure reduces mathematical to a SDOF approximation by assuming its deformed shape, then the solution of the equation of motion is only an approximation of the dynamic behaviour.

The quality of the result obtained with a SDOF approximation depends on many factors. The assumption is good if the physical properties of the system constrain it to move more easily with the assumed shape and if the loading gives a significant

response with this assumed shape. Otherwise, the true behaviour may bear little resemblance to the computed response. One of the greatest disadvantages of the SDOF approximation is that it is difficult to assess the reliablity of the results obtained from it.

The generalized displacement solution is given by,

$$y(x,t) = \phi(x)Y(t), \tag{2.10}$$

where the shape function is designated $\phi(x)$ and the amplitude of the motion is represented by the generalized coordinate $Y(t)$.

2.4.4 Simple Beam Equation

The equation of motion for a simple beam is formulated as a partial differential equation of motion. Its significant physical properties are shown in Figure 2.4(a). It is assumed that the flexural stiffness $EI(x)$ and the mass per unit length $m(x)$ both vary arbitrarily with position x along the span L. The transverse loading $p(x,t)$ and the transverse displacement response $y(x,t)$ are both assumed to vary arbitrarily with position and time.

The partial differential equation of motion is derived by considering the equlibrium of forces acting on the differential segment of the beam shown in Figure 2.4(b) and results in the simple beam equation,

$$\frac{\partial^2}{\partial x^2}\left(EI\frac{\partial^2 y}{\partial x^2}\right) + m\frac{\partial^2 y}{\partial t^2} = p. \tag{2.11}$$

This elementary case of beam flexure is also called the Bernoulli-Euler beam equation and relates the curvature of the beam to the bending moment at each section of the beam.

The simple beam equation is based on the following assumptions.

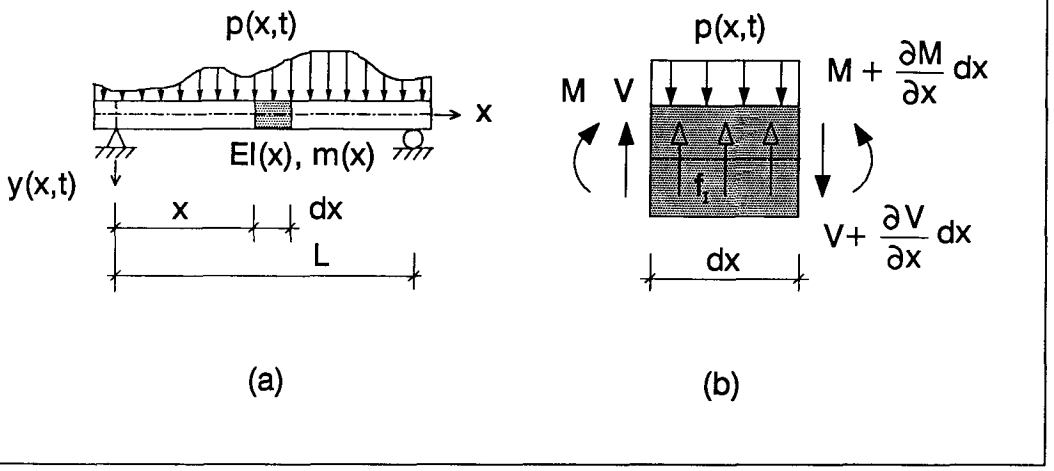

Figure 2.4: Simple beam: (a) properties, (b) differential element.

- The material is homogeneous, isotropic and obeys Hooke's law.
- The beam is straight and has a constant cross section.
- Only small deflections are considered.
- The beam is long compared to the cross-sectional dimensions, and therefore the effect of shear distortion can be neglected.
- Plane sections remain plane, and therefore the effect of cross sectional rotation can be neglected.

2.4.5 Vibration Modes

Shear distortion and rotational inertia were assumed to be negligible together with any axial force effects. The simple beam equation of Equation 2.11 for free vibration is rewritten by using primes to indicate differentiation with respect to x and dots for

differentiation with respect to t and becomes

$$y^{iv} + \frac{m}{EI}\ddot{y} = 0. \tag{2.12}$$

After the generalized displacement expression of Equation 2.10 has been substituted and variables are separated Equation 2.12 becomes

$$\frac{\phi^{iv}(x)}{\phi(x)} + \frac{m}{EI}\frac{\ddot{Y}(t)}{Y(t)} = 0. \tag{2.13}$$

Two ordinary differential equations are obtained, one involving each variable. By simply substituting the initial conditions $Y(0)$ and $\dot{Y}(0)$ of an undamped generalized SDOF system into Equation 2.6, the free vibration solution becomes

$$Y(t) = \frac{\dot{Y}(0)}{\omega}\sin\omega t + Y(0)\cos\omega t. \tag{2.14}$$

The general solution of the shape function is

$$\phi(x) = A_1 \sin ax + A_2 \cos ax + A_3 \sinh ax + A_4 \cosh ax, \tag{2.15}$$

where A_1, A_2, A_3 and A_4 are constant, and a is a variable.

The four boundary conditions for the simply supported beam with uniform properties are as follows.

at $x = 0$:	$\phi(0) = 0$	- zero deformation at left support
	$M(0) = EI\phi^{ii}(0) = 0$	- zero moment at left support
at $x = L$:	$\phi(L) = 0$	- zero deformation at right support
	$M(L) = EI\phi^{ii}(L) = 0$	- zero moment at right support

Simple substitution of the boundary conditions results in the frequency equation and consequently the vibration shape for the n mode, which are

$$\omega_n = n^2\pi^2\sqrt{\frac{EI}{mL^4}} \quad \text{and} \quad \phi_n(x) = A_1 \sin\left(\frac{n\pi x}{L}\right) \tag{2.16}$$

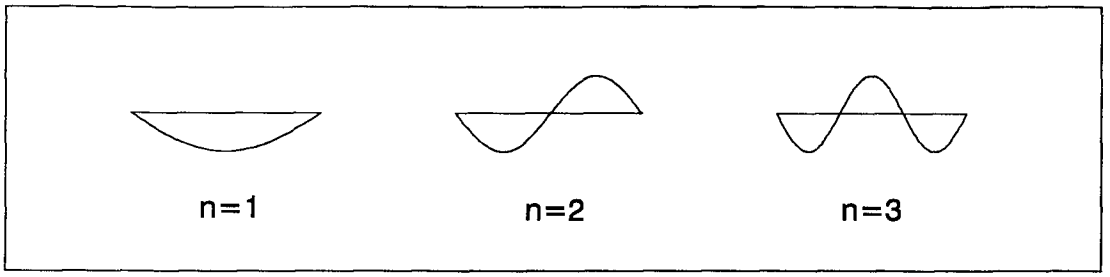

Figure 2.5: First three vibration modes for simple beam vibration analysis.

respectively. The constant A_1 is arbitrary and is selected to satisfy the actual test conditions. Results for the first three modes of vibration are shown in Figure 2.5, where n is the mode number.

2.4.6 Timoshenko Beam Equation

If the effect of rotation of the cross section and the shear distortion are considered in the equilibrium of forces acting on the differential element, and if the axial forces still are neglected, the equation of motion becomes

$$\underbrace{EI\frac{\partial^4 y}{\partial x^4} - \left(p - m\frac{\partial^2 y}{\partial t^2}\right)}_{\text{elementary case}} - \underbrace{mr^2\frac{\partial^4 y}{\partial x^2 \partial t^2}}_{\text{rotational inertia}} + \underbrace{\frac{EI}{k'AG}\frac{\partial^2}{\partial x^2}\left(p - m\frac{\partial^2 y}{\partial t^2}\right)}_{\text{shear distortion}} + \underbrace{-\frac{mr^2}{k'AG}\frac{\partial^2}{\partial t^2}\left(p - m\frac{\partial^2 y}{\partial t^2}\right)}_{\text{combined shear distortion and rotational inertia}} = 0. \quad (2.17)$$

The radius of gyration r^2 of the cross section is I/A, $k'A$ represents the effective shear area of the section, for a rectangular section k' is $5/6$, and G is the shear modulus. In the Timoshenko beam equation, Equation 2.17, it is possible to identify the various terms which are associated with the elementary formulation and with the additional effects of shear distortion and rotational inertia.

2.4.7 Effects of Shear Deformation and Rotatory Inertia

From the Timoshenko beam equation the effects of rotational motion and shearing force is derived for a simply supported beam with a sinusodial vibration shape. The frequency expression is approximated as,

$$\omega_n \doteq n^2\pi^2 \sqrt{\frac{EI}{mL^4}\left[\frac{1}{1+\left(\frac{n\pi r}{L}\right)^2\left(1+\frac{E}{k'G}\right)}\right]}, \tag{2.18}$$

in which the term in the square brackets provides the correction factor for shear and rotatory inertia. For a rectangular section a value of 3 for the term $E/k'G$ is valid for a beam of 'typical' material, but is very conservative for wood and timber material. A very rough estimate of $E/k'G$ for wood material gave a value of 18. It is evident that this correction increases as the mode number increases and as the slenderness ratio L/r decreases.

2.4.8 Ramp Loading

A drop-weight impact machine induce a single blow impact to the beam together with an initial velocity. This initial velocity depends upon the height at which the impact hammer is dropped. After contact the beam and the hammer travel together until the beam fails unless the drop-height used 'just' caused the beam to fail. The contact force between the hammer and the beam is recorded by the loadcell of the impact hammer assembly.

Preliminary impact tests performed for this investigation indicated that the contact force could be modelled as a unsymmetric triangular pulse with a rise time followed by an instantaneous vertical decay. The rise time of the load is denoted as t_1. This type of load is called ramp loading and is illustrated in Figure 2.6.

The ramp load response is divided into two phases. Phase 1, also called the pulse phase, corresponds to the interval during which the load acts. It is followed by

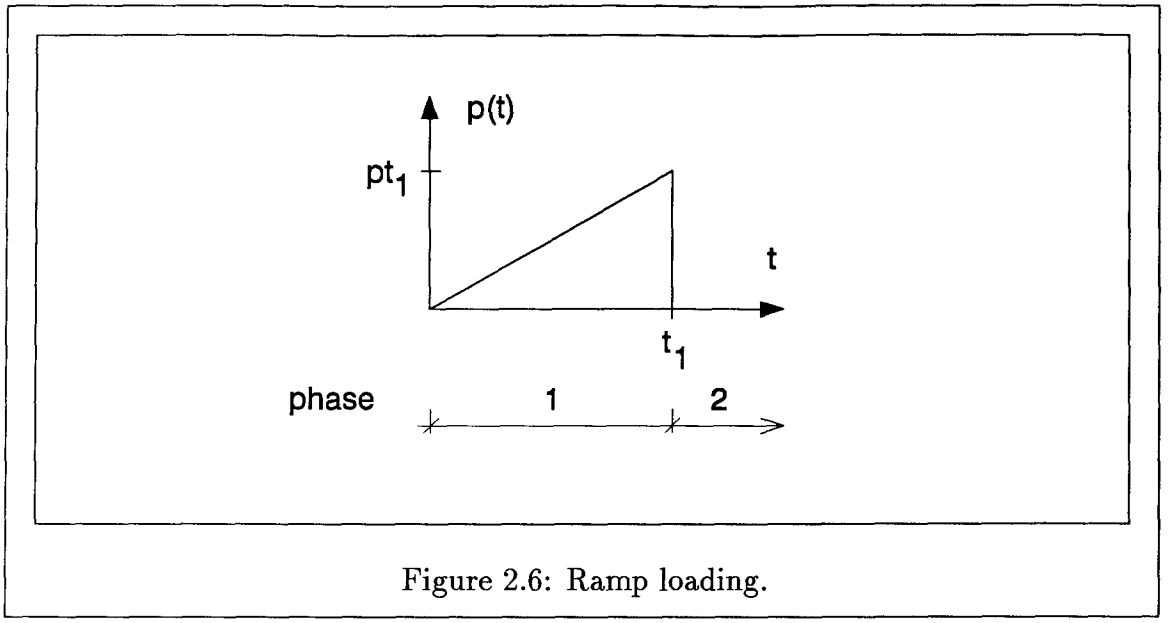

Figure 2.6: Ramp loading.

phase 2, also called the free-vibration phase. The ramp load is expressed as a single analytical function which has a closed-form solution.

During phase 1 the forced vibration is given by the specific ramp load

$$p(t) = pt_1 \frac{t}{t_1}, \tag{2.19}$$

where pt_1 is the load at the end of phase 1 at time t_1.

In phase 2 the response is a free-vibration response and generally follows the free-vibration of Equation 2.6. However the response for phase 2 is assumed to have no relevance to this investigation, because the ramp load drops to zero as the beam fails.

2.4.9 Earlier Analysis

The analysis used in earlier impact tests at UBC (Bentur et al., 1986), which was defined as the earlier analysis, required loadcell measurements over the time and measurements from at least one accelerometer mounted on the beam during the test event for each specimen. The distribution of acceleration along the beam has to be assumed in order to implement the concept of generalized inertia load acting at the

centre of the beam. The generalized inertia load concept is explained in more detail in the following section.

The beam is modelled as a SDOF system where the actual bending load is evaluated by subtracting the generalized load from the loadcell measurements. The failure stress is finally calculated from the actual bending load by application of the static failure stress given in Equation 2.1 where P_{max} is the actual failure bending load.

2.4.9.1 Generalized Inertia Load

The concept that a mass develops an inertial force proportional to its acceleration and opposing its direction, is known as d'Alembert's principle. If this principle is applied to a generalized SDOF system, the distributed inertial force f_I becomes

$$f_I = m\frac{\partial^2 y(x,t)}{\partial t^2}, \tag{2.20}$$

where m is the distributed mass along the beam and $\partial^2 y(x,t)/\partial t^2$ is the distribution of acceleration along the beam.

The principle of virtual displacement states that if a system in equilibrium is subjected to a virtual displacement the total work done by the forces will be zero. The virtual work done by the generalized inertial load $P_I(t)$ at the midspan of the beam is equal to the virtual work done by the distributed inertial forces f_I along the beam. When the virtual work expression is formulated, advantage is taken of the symmetry of the simply supported beam that has a clear span of L.

$$P_I(t)\delta Y = 2\int_0^{L/2} f_I \delta y dx = 2\int_0^{L/2} m\frac{\partial^2 y(x,t)}{\partial t^2}\delta y dx, \tag{2.21}$$

in which

$$\delta y = \phi(x)\delta Y, \tag{2.22}$$

where δy is the distribution of virtual displacement along the beam and δY is the virtual displacement at the midspan of the beam. The generalized inertial load at

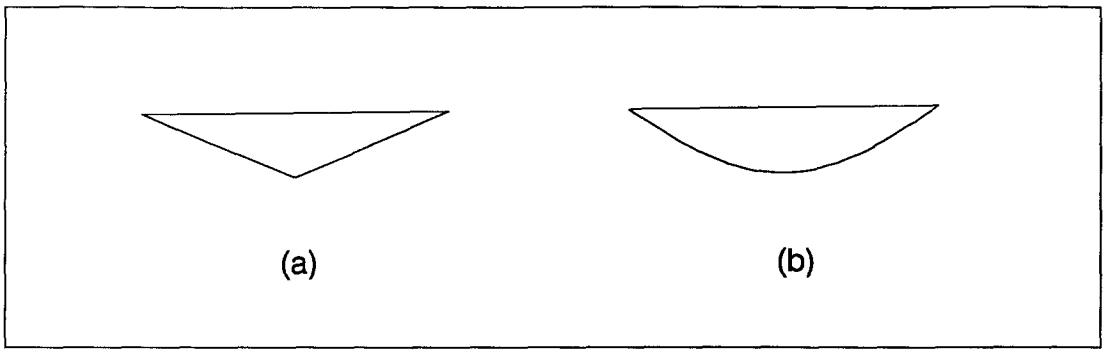

Figure 2.7: Distributions of displacement: (a) bi-linear, (b) sinusodial.

the midspan becomes

$$P_I(t) = 2m\ddot{Y}(t) \int_0^{L/2} [\phi(x)]^2 \, dx, \tag{2.23}$$

where $\ddot{Y}(t)$ is the acceleration over time at the midspan of the beam and $\phi(x)$ is the shape function of the beam. The shape function gives the distribution of acceleration along the beam. It is assumed that accelerations have the same distribution along the beam as displacements. The distributions of displacement, and hence the distributions of acceleration, and consequently the distributions of virtual displacement are assumed to be bi-linearly distributed or sinusodially distributed along the beam, as shown in Figure 2.7.

The generalized inertial loads becomes

$$Pl_I(t) = \frac{mL}{3}\ddot{Y}l(t) \quad \text{and} \quad Ps_I(t) = \frac{mL}{2}\ddot{Y}s(t), \tag{2.24}$$

where l indicates the bi-linear distribution and s indicates the sinusodial distribution. The acceleration at the middle of the span become

$$\ddot{Y}l(t) = \frac{\ddot{Y}_i(t)L}{2x_i} \quad \text{and} \quad \ddot{Y}s(t) = \frac{\ddot{Y}_i(t)}{\sin\left(\frac{\pi x_i}{L}\right)}, \tag{2.25}$$

where $\ddot{Y}_i(t)$ are the accelerometer readings from the ith accelerometer at the distance x_i from the closest support. The generalized load expressions for the bi-linear

distribution and the sinusodial distribution becomes

$$Pl_I(t) = \frac{mL^2\ddot{Y}_i(t)}{6x_i} \quad \text{and} \quad Ps_I(t) = \frac{mL\ddot{Y}_i(t)}{2\sin\left(\frac{\pi x_i}{L}\right)} \tag{2.26}$$

respectively. The location of the accelerometer is important for the reliability of the distribution assumption, and will be discussed later. In the simple beam theory the beam is assumed to have a sinusodial displacement distribution.

The derivation above shows how the distributed inertial forces are replaced by a generalized inertia load acting at the centre of the beam. The beam is then modelled as a SDOF system and the actual bending load is evaluated by subtracting the generalized inertial load from the loadcell measurements. The failure stress is finally calculated from the actual bending load by application of the maximum bending stress Equation 2.1 for static analysis.

2.4.10 FENTAB Analysis

A finite element program called FENTAB (Finite Element Nonlinear Transient Analysis of Beams) Version 1.0 is capable of numerically simulating the static and transient response of Bernolli-Euler beams or simple beams exhibiting large deformations and elastic-plastic behaviour (Folz, 1986). The FENTAB program was employed in various parametric studies regarding the non-linear response of slender ductile beams to air-blast pressure pulses.

The following numerical solution algorithm is used in the computer program FENTAB. The spatial domain of the beam is discretized into a number of individually identical subdomains called finite elements. The differential equation of motion is formulated with the principle of virtual work, and is solved by the central difference method. The varables in the differential equation of motion are formulated in a consistent manner. The central difference method adopts displacement expressions

for the integration scheme. The FENTAB analysis requires loadcell measurements over time for each test and knowledge of the modulus of elasticity for each specimen.

In this investigation the material is assumed to have a brittle failure and consequently have a elastic behaviour before failure. The full potential of the FENTAB program was therefore not used. The failure stress f_{max} is calculated from the strain ϵ at the middle of the beam, as

$$f_{max} = E\epsilon, \tag{2.27}$$

where E is the modulus of elasticity.

2.4.11 Modal Analysis

The dynamic solution of the beam is found by using the mode-superposition analysis (Clough and Penzien, 1985) and is defined as the modal analysis. The properties of the beam are distributed along the beam and the beam is therefore a distributed-parameter system. The beam is modelled as a generalized single-degree-of-freedom (SDOF) system by deriving the partial differential equation of motion for the simple beam flexure.

The modal analysis requires loadcell measurements over time for each test and that the modulus of elasticity is known for each specimen. The stresses in the beam are then calculated using assumptions regarding the load-time relationship and the deflected shape of the beam. These assumptions are based on test results. The failure stress is calculated from the failure moment according to Equation 2.1.

The modal analysis is carried out according to the following steps.

Step 1: Compute Mode Shapes and Frequencies (section 2.4.11.1).

Step 2: Compute Generated Mass and Loading (section 2.4.11.2).

Step 3: Solve the Normal-Coordinate Response Equation (section 2.4.11.3).

Step 4: Evaluate Displacement Response (section 2.4.11.4).

Step 5: Evaluate Dynamic Beam Moments (section 2.4.11.5).

2.4.11.1 Compute Mode Shapes and Frequencies

The first step in the modal analysis is to evaluate the undamped vibration mode shapes and frequencies. This step is covered in section 2.4.5.

2.4.11.2 Compute Generalized Mass and Loading

The second step of the modal analysis includes the essential operation which transforms the geometric displacement coordinates to the modal-amplitude or normal coordinates. Any displacement shape is developed by superposing suitable amplitudes of the modes of vibration. These modal amplitudes or normal coordinates are therefore associated with the mode shapes of the structure.

The simple beam equation is decoupled if Betti's law is applied on the two orthogonality relationship of the distributed-parameter system. The decoupling results in

$$M_n\ddot{Y}_n(t) + \omega_n^2 M_n Y_n(t) = P_n(t), \tag{2.28}$$

where

$$M_n = \int_0^L \phi_n^2 m(x)dx \quad \text{and} \quad P_n(t) = \int_0^L \phi_n(x)p(x,t)dx \tag{2.29}$$

are the generalized mass and the generalized loading associated with the generalized mode shape ϕ_n respectively.

2.4.11.3 Solve the Normal-Coordinate Response Equation

The third step of the modal analysis is solved in section 2.4.8. The total response for phase 1 is the solution of the normal-coordinate response equation.

2.4.11.4 Evaluate Displacement Response

A distributed-parameter system, such as the simple beam, has an infinite number of vibration shapes as indicated in Equation 2.16. In this equation the constant A_1 is arbitrary. In the modal analysis this constant is absorbed by the other constants in the modal response expression of Equation 2.30. Therefore the constant A_1 is set equal to 1 in the following analysis (Paz, 1985). Any physically permissible displacement pattern is made up by superposing appropriate amplitudes of the vibration mode shapes for the structure and becomes

$$y(x,t) = \sum_{n=1}^{\infty} \phi_n(x) Y_n(t). \tag{2.30}$$

The displacement of the midspan point of loading is obtained by letting $x = L/2$.

The fourth step in the modal analysis is achieved by substituting expressions for the shape function and the ramp load response with the normal coordinate expression of Equation 2.30. The complete derivation is given in Appendix A. If the dynamical system is considered to be undamped and the initial displacement is set equal to zero the displacement response of Equation 2.30 becomes

$$y\left(\frac{L}{2}, t_1\right) = \sum_{n=1}^{\infty} \sin\left(\frac{n\pi}{2}\right) \left[\frac{2\dot{y}(0)}{\omega_n n\pi}(\cos(n\pi) - 1)\sin(\omega_n t_1) + \right.$$
$$\left. + \frac{2pt_1 \sin\left(\frac{n\pi}{2}\right)}{mL\omega_n^2}\left(1 - \frac{\sin(\omega_n t_1)}{\omega_n t_1}\right)\right], \tag{2.31}$$

at the midspan point ($x = L/2$) and at the failure time t_1. Similarly the dynamic displacements of the structure can be evaluated at any time.

2.4.11.5 Evaluate Dynamic Beam Moments

At any time the internal forces in the structure are found by applying the structure force-displacement relationships. The fifth step in the modal analysis is accomplished

by using the basic moment-curvature relationship from the elementary beam theory,

$$M(x,t) = EI\frac{\partial^2 y(x,t)}{\partial x^2}, \tag{2.32}$$

in which the internal moment $M(x,t)$ is proportional to the curvature of the beam $\partial^2 y(x,t)/\partial x^2$. The failure moment is assumed to occur at the mid-point ($x = L/2$) and at the failure time ($t = t_1$).

The failure stress is calculated from Equation 2.1 by substitution of the failure moment and becomes

$$\sigma\left(\frac{L}{2}, t_1\right) = \frac{Ed\pi^2}{2L^2}\sum_{n=1}^{\infty} n^2 \sin\left(\frac{n\pi}{2}\right)\left[\frac{2\dot{y}(0)}{\omega_n n\pi}(\cos(n\pi) - 1)\sin(\omega_n t_1) + \right.$$
$$\left. + \frac{2pt_1 \sin\left(\frac{n\pi}{2}\right)}{mL\omega_n^2}\left(1 - \frac{\sin(\omega_n t_1)}{\omega_n t_1}\right)\right], \tag{2.33}$$

at the mid-point ($x = L/2$) and at the failure time t_1.

2.5 Statistical Analysis

Data or measurements generated from tests do not describe a quantity that has a deterministic value. Instead the measurements are probabilistic and have an inherent variation. The distribution of measurements was assumed to be a normal distribution. The sample distribution was created from the cumulative frequecency of each quantity.

A better representation of the actual properties might be given by non-parametric percentiles. The non-parametric 50th percentile was used as another central tendency property. Three values above and below the 50th percentile of the cumulative frequency distribution were weighted differently. The values closest to the 50th percentile were given the weight 25.0 %, the values furthest from the 50th percentile were given the weight 8.3 % and the values in between were given the weight 16.7 % (Bury, 1979). The non-parametric average of these weighted values was calculated and was assumed

to represent the non-parametric 50th percentile. In the same way, the non-parametric 25th percentile was computed to give an indication of the lower end of the sample distribution. The failure stress values calculated by the modal analysis was used to create the sample distribution of failure stress.

2.6 Response to Impulsive Loads

An impact occurs when two or more bodies collide. An important characteristic of impact is that the forces on and within the bodies are generated over a very short period of time. Such forces sometimes are referred to as impulse-type forces (Harris, 1988).

Impulsive load or impact load is defined as a load applied during a relatively short time interval that also produce an instaneous change in velocity. The maximum response to an impulsive load is reached in a very short time before the damping forces can absorb much energy. For this reason only the undamped response to impulsive loads is considered in this section on impulsive loads.

The impulse duration ratio is the ratio between the impulsive load duration t_1 and the fundamental or natural period of the structure T. The response ratio and response spectra are presented for various impulsive loads in the following sections. Both impulse duration ratio and response ratio are very useful in discussions about response of impulsive loads.

2.6.1 Response Ratio

The response ratio provides a convenient measure of the influence of the dynamic character of the loading. The response ratio is the ratio between the dynamic response at any time divided by the static response (Clough and Penzien, 1985). This ratio is

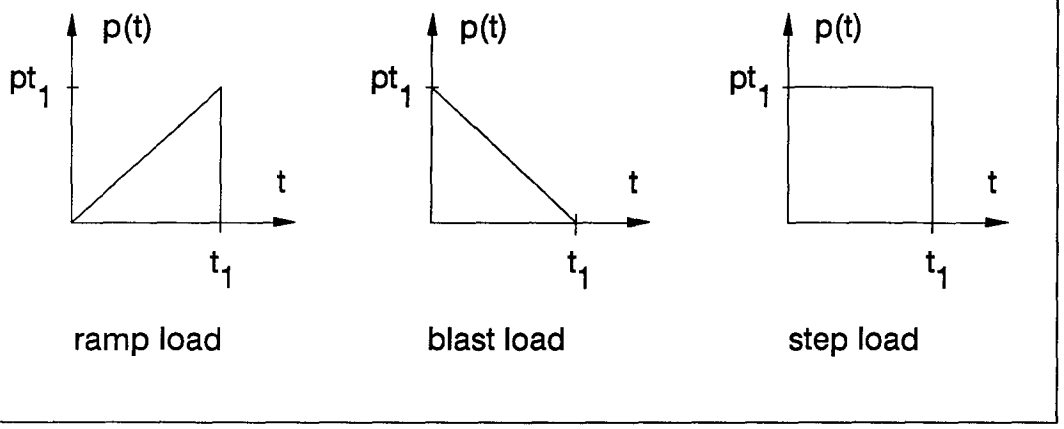

Figure 2.8: Three different types of impulsive loads.

also called the dynamic load factor (Paz, 1985).

The dynamic magnification D is not the same as the response ratio. The dynamic magnification factor is the ratio of the maximum displacement of a system excited by a harmonic force to the displacement of a system excited by a force applied static of the same magnitude as the harmonic force.

In this thesis the strength ratio was defined as the ratio between the dynamic failure stress and the static failure stress. Three types of impulsive loads presented in this thesis are the ramp, blast, and step load. They are shown in Figure 2.8.

The failure is assumed to occur at the end of the pulse era at time ($t = t_1$). Consequently the strength ratio of interest is the strength ratio $R(t_1)$. The strength ratio $R(t_1)$ is conveniently expressed in form of the impulse duration ratio (t_1/T) by substituting $\omega = 2\pi/T$. In Appendix B the strength ratios $R(t_1/T)$ are derived for the three types of impulsive loads, and they become:

$$\text{ramp:} \qquad R(t_1/T) = 1 - \frac{T}{2\pi t_1} \sin\left(\frac{2\pi t_1}{T}\right) \tag{2.34}$$

$$\text{blast:} \quad R(t_1/T) = \frac{T}{2\pi t_1} \sin\left(\frac{2\pi t_1}{T}\right) - \cos\left(\frac{2\pi t_1}{T}\right) \tag{2.35}$$

$$\text{step:} \qquad R(t_1/T) = 1 - \cos\left(\frac{2\pi t_1}{T}\right). \tag{2.36}$$

The strength ratio is used to create the response spectra of the impulsive loads.

2.6.2 Response Spectra

The response spectra or spectrum of impulsive loads is used to predict, with necessary engineering accuracy the maximum effect to be expected on a simple structure. A comparison plot of the different response spectra is created from the strength ratios $R(t_1/T)$ for the three loading types. In Figure 2.9 the strength ratios for each of the loading types are plotted against the impulse duration ratio (t_1/T). This figure shows how important a proper determination and characterization of the loading type is on the dynamic response.

2.7 Summary

The effect of the time-history of loading and the inertia effect of the structure are considered in dynamic analysis. The static analysis was used both for comparative purposes and for computing the modulus of elasticity. The stress wave analysis was employed to assure that applied load could be considered to be transferred into stresses instantaneously all over the beam. Preliminary impact tests performed in this investigation indicated that the contact force between the impact head and the beam could be modelled as a ramp load, with an initial velocity imported to the mid-point of the beam.

The dynamic anlysis was approached with thress different analyses. The analysis used in earlier impact tests at UBC was based on a generalized load assumption and required accelerometer measurements. The FENTAB analysis employed a very detailed finite element program which would be inefficiently used in this investigation.

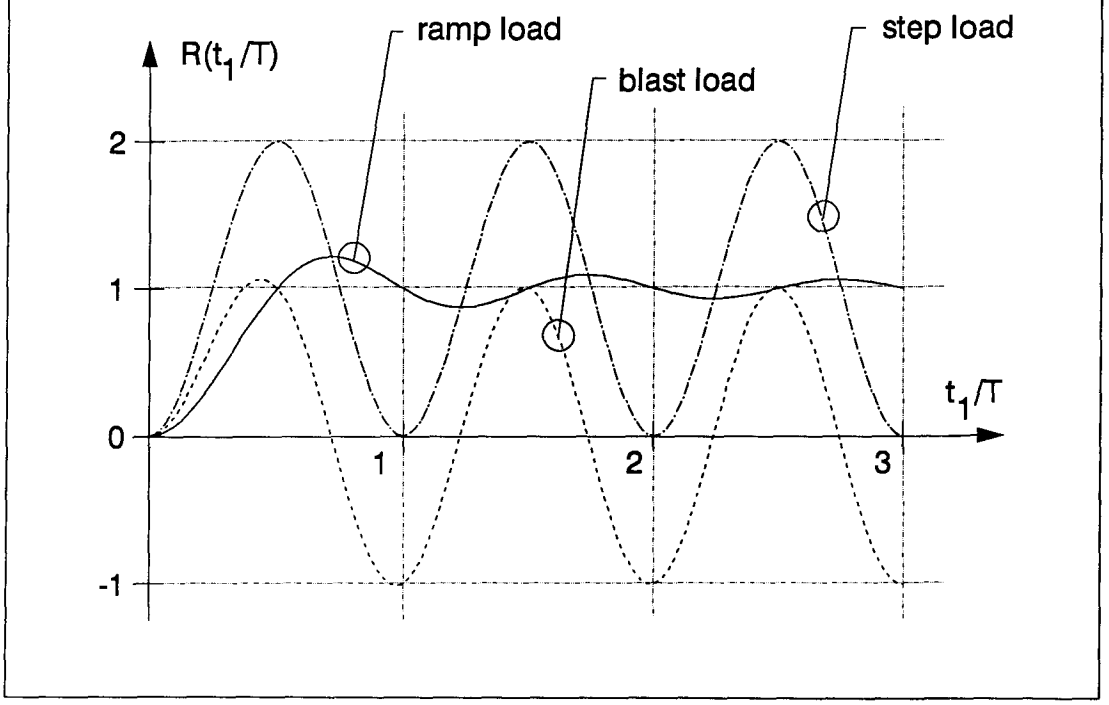

Figure 2.9: Response spectra of three different types of impulsive loads.

The modal analysis was a mode-superposition analysis of a distributed-parameter system, and its solution was easily divided into its static and dynamic parts.

The strength ratio was defined as the ratio between the dynamic failure stress and the static failure stress. The importance of proper determination and characterization of the impact loading was shown with a response spectra.

Chapter 3

Experimental Aspects

3.1 Introduction

This chapter presents the experimental approach taken to solve the problem addressed in this thesis. Both static and impact tests were performed at different loading rates to understand and quantify the differences between static and impact loading. The static tests were conducted with a MTS set-up, from MTS System Corporation in Minneapolis, Minn., USA, mounted in a test frame. The impact tests were done with an instrumented drop-weight impact machine designed by Professor S. Mindess and built at the Department of Civil Engineering at the University of British Columbia (UBC). Both testing machines were located in the Structural Laboratory of the Department of Civil Engineering at UBC.

Before a specimen was tested to failure by either static or impact loading it was non-destructively tested in a static test set-up and the modulus of elasticity was computed. The same static apparatus was used as was employed for the static failure tests. The modulus of elasticity was used to group the specimen into various loading rate groups.

The chapter starts by outlining the two test set-ups. This is followed by a description of loading rates, sampling rates, specimens, sample sizes and grouping of specimens. The various types of failure mode recordings are presented at the end of the chapter.

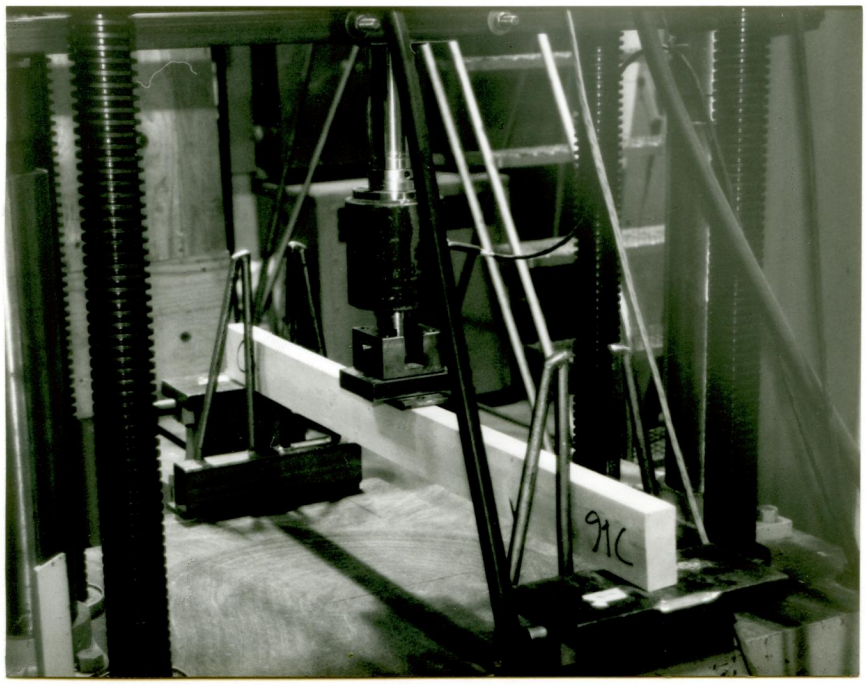

Figure 3.1: Static test set-up.

3.2 Static Test Machine

A test frame was used for mounting a MTS loading jack which was connected to a MTS control unit. Figure 3.1 shows the static test set-up. A schematic drawing of the static testing set-up is provided in Figure 3.2, where the various parts are identified.

The MTS loading jack was hung vertically in the locked crosshead of the test frame, and was balanced against horizontal movement with a steel bar system attached to the columns of the test frame. The MTS testing system was hydraulically controlled. Detailed data on the static test machine are given in Appendix C, together with a description of the calibration procedure for the static test machine.

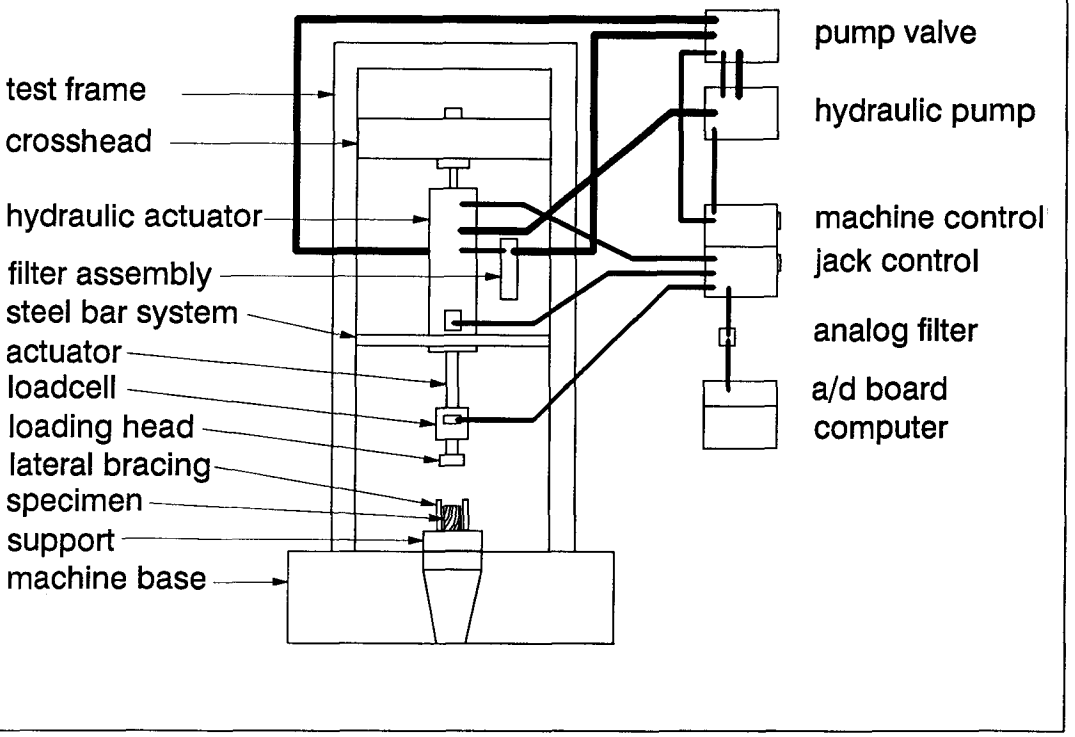

Figure 3.2: Schematic drawing of static test set-up.

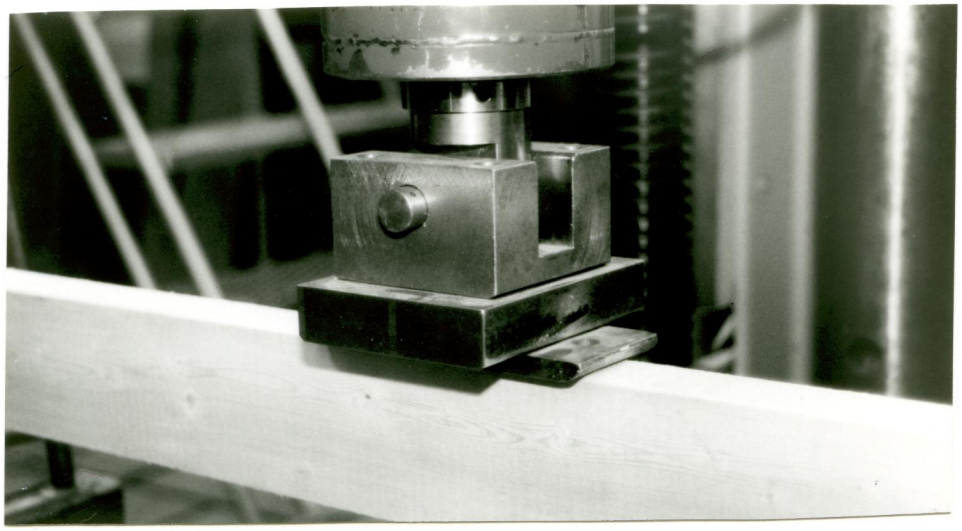

Figure 3.3: Static loading head.

The MTS material testing generator (model 340) and the MTS machine control unit (model 436) controlled the whole MTS set-up. The MTS jack controller (model 406) regulated the loading jack and allowed the applied loading to be both load and deformation controlled.

A loading head with a steel plate was mounted on the actuator. The supports on the base of the test frame were used as supports for the beam specimen. Steel plates were mounted on the supports to prevent indention and allowed rotation of the beam at its supports. Photographs shows the details of the static loading head, Figure 3.3 as well as of the support used in the static testing set-up, Figure 3.4. The lateral bracing close to the support seen in Figure 3.4 did not have any influence on the specimen performance during tests because no contact occurred between the specimen and the bracing.

Figure 3.4: Static support.

The contact force between the loading head and the test specimen was measured by a MTS loadcell (model 661.21-02) with built-in strain gauges. It was assumed that the contact force represented the load experienced by the beam. The displacement of the actuator was assumed to represent the mid-point displacement of the beam. The mid-point displacement measurements ranged between 8.6 mm and 28.7 mm. The displacements at the supports was less than 0.5 mm, and were therefore assumed to be negligible.

Both the measurements of the load and displacement were recorded in volts and their output signal was filtered through an analog low-pass filter of 482 Hz. The static loading event consisted essentially of low frequency signals. High frequency components were therefore of no consequence to the test results and could be eliminated by this low-pass filter.

The analog-digital board (A/D board) converted the filtered analog voltage signal into a digital signal before the signal entered the computer. The digital signal was stored in the hard drive of the computer with the data collecting program Labtech Notebook version 4, a software by Laboratory Technologies Corporation in Wilington, Mass., USA. Each computer file was given a name corresponding to the specimen tested.

3.3 Impact Test Machine

The impact test machine used was the same instrumented drop-weight impact machine used in earlier impact tests at UBC, see section 1.2.4. Figure 3.5 shows the impact test set-up. A schematic drawing of the impact machine is provided in Figure 3.6, where the various parts are identified.

In the impact tests the load was measured by a loadcell mounted on the lower part of the drop-weight hammer. The mechanical part of the impact machine was

Figure 3.5: Impact test set-up.

controlled by the panel of the machine control. The data acquisition system was controlled by the keyboard of the connected computer. The hammer was raised to the desired drop-height with the hoist by an electric motor. The hydraulic brakes were applied. The pin, which connect the hoist with the hammer, was released and the data acquisition system was activated. When the brakes were released the hammer commenced a free fall. The fall of the hammer was guided by the two columns. Some friction was introduced on this free-fall. If the specimen did not fail at the first impact the hydraulic brakes were manually triggered to grab the impact hammer to prevent multiple impacts.

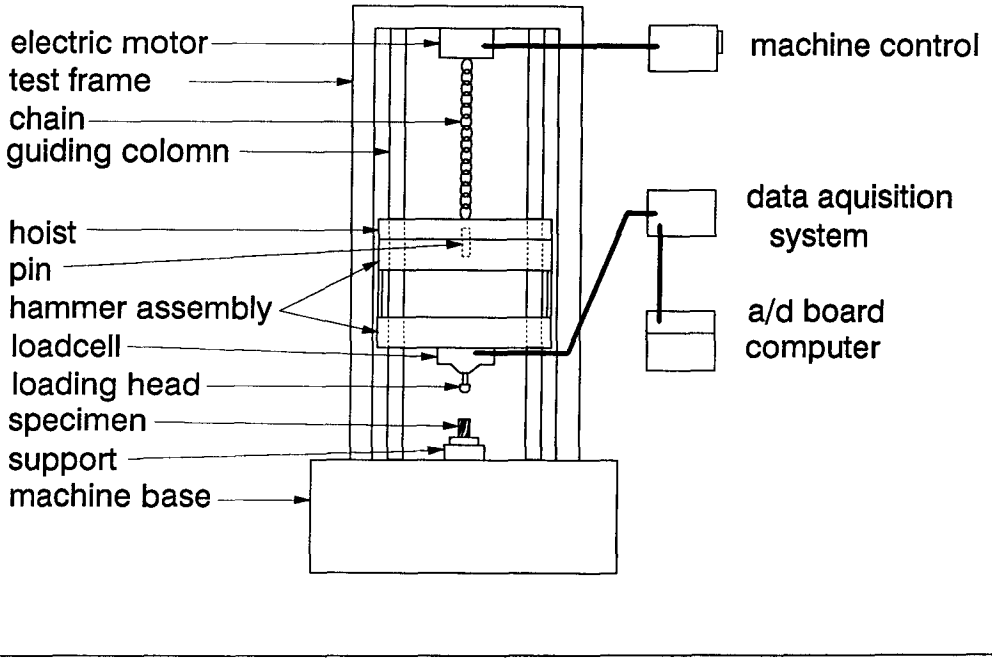

Figure 3.6: Schematic drawing of impact test set-up.

3.3.1 Impact Loadcell

The striking head attached to the loadcell was an assembly made out of a steel block with a screw-bolt at its impacting end. A strain gauge was connected at the top of the bolt against the steel block. Some data of the impact loadcell used for the impact tests are given in Appendix C, together with a description of the calibration procedure for the impact test machine.

A half-sphere was screwed to the end of the screw-bolt and was tighten from above by a nut. Figure 3.7 shows the whole impact loadcell assembly.

The loadcell assembly was manufactured by Budd Instrument Ltd., Ont., Canada, except for the half-sphere at the impacting end, which was manufactured by the workshop at the Department of Civil Engineering at UBC. When a load was applied to the loadcell the strain gauge became unbalanced and produced an output voltage signal.

The indentation and penetration problem from earlier impact tests at UBC were solved by using a steel plate (64 x 152 x 10 mm) with rounded edges. In Figure 3.7 this steel plate is seen placed between the loadcell and the specimen. The loading conditions of the static set-up were intended to be comparable with the loading conditions of the impact set-up. The same steel plate was therefore screwed on to the MTS loading head for both the modulus of elasticity tests and the static tests, as shown in Figure 3.3. Figure 3.8 shows one of the impact supports on which a steel plate was placed to allow rotation of the beam.

3.3.2 Accelerometer

The earlier analysis, which was used for the earlier impact tests at UBC, required that the acceleration be measured at a minimum of one point along the beam during testing. On some of the specimen accelerometers were mounted at three locations

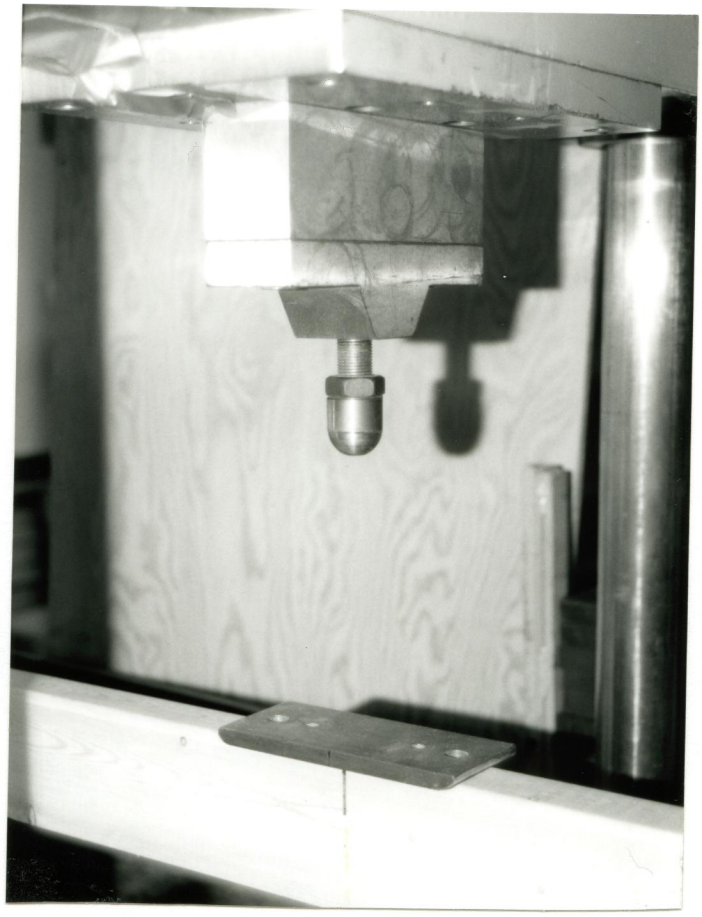

Figure 3.7: Impact loadcell assembly.

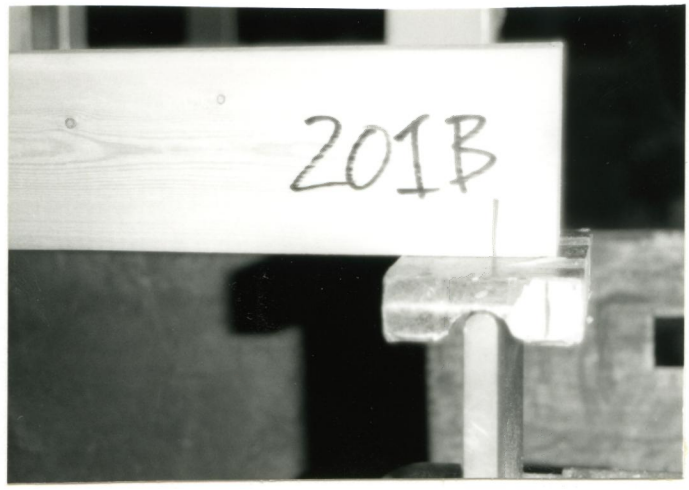

Figure 3.8: Impact support.

along the top of the half span of the beam. The acceleration over time was measured.

The accelerometers employed were of the piezoelectric sensor type or the quartz type (model 302A). They were manufactured by PCB Piezoelectronics Inc., N.Y., USA. The accelerometers were specified by the manufacturer to follow long duration shock events of up to 20 msec duration and to offer good low frequency response. They were screwed into small plastic bases which were glued on the specimens with epoxy glue. A study of accelerometer measurements showed a significant drift in voltage when measurements had been collected for more than 50 msec.

3.3.3 Data Acquisition Unit

The analog voltage signals obtained from the loadcell and the accelerometers were fed into the data acquisition unit, as shown schematically in Figure 3.6. The data aquisition system worked like a signal conditioner and amplified the loadcell signal.

The accelerometers had a separate amplification unit. The data acquisition unit also had the ability of filtering the incoming analog signals. However, such filtering had a detrimental effect on these signals, and changed the amplitude of the signals. It was therefore decided to collect the raw signals and carry out digital filtering of the data later to obtain more reliable test results.

From the data aquisition system the signal was transferred into the A/D board, which transformed the analog signal into a digital signal. A personal computer was connected to the data aquisition system. The computer had a random access memory (RAM) of 256K. The data collecting software employed was Computerscope ISC-16 purchased from PC Electronics Inc., Calif., USA. This software worked like a digital oscilloscope and it had features similar to an analog oscilloscope.

3.3.4 Acceleration of the Impact Hammer Assembly

The friction from the columns of the impact machine decreased the acceleration of the hammer to less than the acceleration due to gravity (9.81 m/sec^2). A few gravity tests were performed with an accelerometer screwed on one end of the hammer assembly. The drop-height was 1 m from the level of where the specimen would be impacted. The hammer dropped that distance in 0.3-0.4 sec and after that distance had a velocity of approximately 4 m/sec. The hydraulic system of the brakes introduced a time delay of about 40 msec between the release of the two brakes, in other words the brakes were not released at the same time. This realization and the fact that the accelerometers were not stable for an event longer then 20 msec implied that the test results from these gravity test were not reliable. Earlier impact tests had found that the acceleration of the hammer after the columns were cleaned with acetone was approximately 9.60 m/sec^2 and after repeated use 8.64 m/sec^2 (Banthia, 1987). An acceleration of the hammer assembly of 8.6 m/sec^2 seemed to be a reasonable value

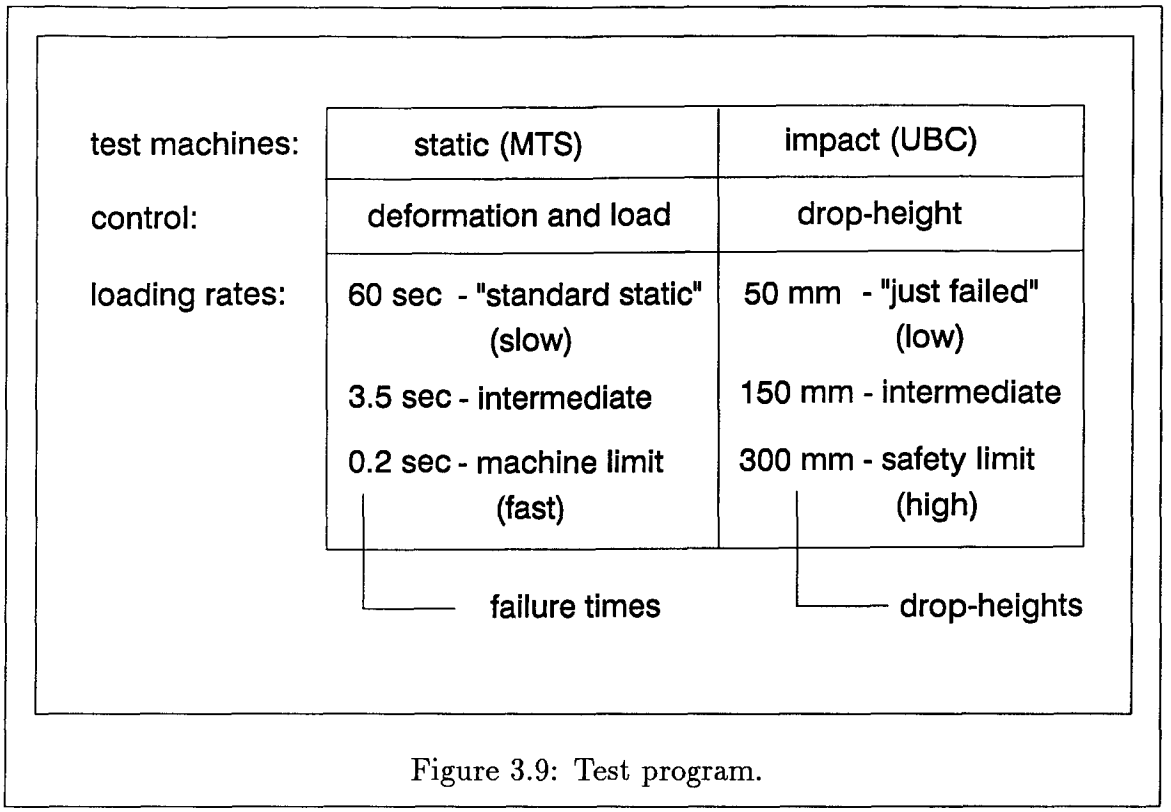

Figure 3.9: Test program.

for these impact tests. The columns were cleaned on the average after every 15 tests.

3.4 Test Program

Nine different loading rates were used to make it possible to understand and quantify the differences between static and impact loading. Figure 3.9 gives a summary of the test program and indicates the different static and impact loading rates. Three static loading rates were used for each of the load controlled tests and the deformation controlled tests. Three impact loading rates were used for the impact tests.

The static tests were intended to be performed in a way that would be comparable to the impact tests. The MTS set-up, used for the static tests, could be run either at a constant deformation rate or at a constant loading rate. Figure 3.10 illustrates the basic difference between the constant deformation rate and the constant loading

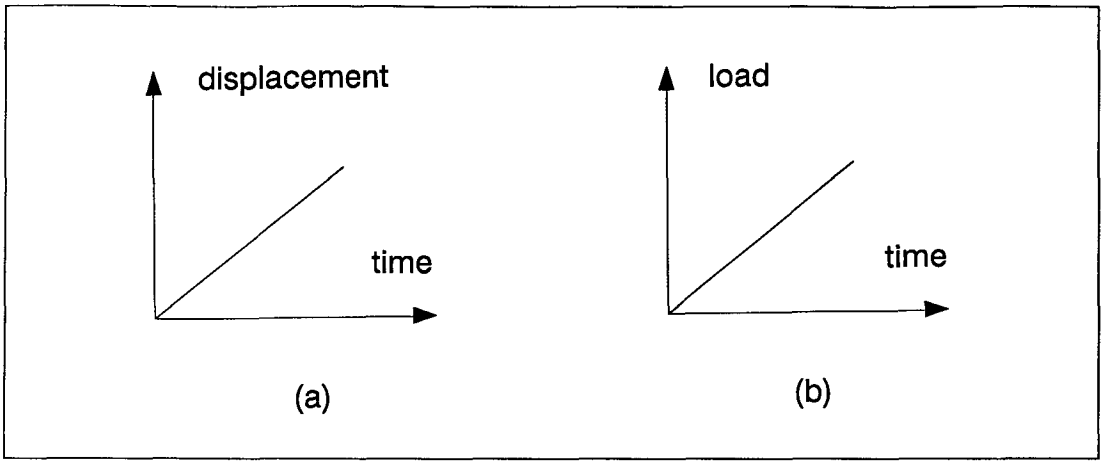

Figure 3.10: (a) constant deformation rate, (b) constant loading rate.

rate.

Constant deformation rate means that the loadcell, and consequently the beam, is moving with a constant velocity. Thus the velocity at any point of the beam would remain the same during the whole impact event. If an impact test was more like the constant loading rate than the constant deformation rate, a plot of the load from the impact loadcell versus time would be linear. The loading event with constant loading rate was stopped by the MTS set-up, as soon as the load was not able to continue to increase with the prescribed loading rate. This breakpoint was the presumed maximum load or failure load.

Preliminary impact tests with three accelerometers mounted on the top of the beam performed during this investigation did not indicate whether a drop-weight impact test could be said to be similar to a constant loading rate or a constant deformation rate. The velocity at any of the three points of the beam did not drastically change. The plots of load versus time very strongly indicated that the impact event predominately was like a constant loading rate test. In spite of the later observation it was decided to be perform the static tests both load and deformation controlled.

The method of load application was studied with regard to failure strength by using different bending test set-ups (Madsen and Mindess, 1986). The difference in strength between different loading systems was found to be strength dependent and most pronounced at the weak end of the failure strength distribution. The deformation controlled tests gave 30 % higher strength value at the 5th percentile and 10 % higher strength value at 25th percentile compared to load controlled tests.

3.4.1 Static Loading Rates

The static tests performed with the MTS set-up were both constant deformation rate controlled and constant load rate controlled. A loading rate which gave a failure time of approximately 60 sec was chosen as the slowest loading rate for the static tests. This slow static loading rate was assumed to represent a 'standard static' test which gave the standard short term failure strength. Preliminary static tests performed for this investigation gave a failure time of approximately 0.2 sec as the fastest mechanically feasible loading rate for the static set-up. The logarithmic average of the estimated slowest and fastest failure times granted an intermediate estimated failure time of approximately 3.5 sec.

3.4.2 Impact Loading Rates

Three different levels of energy were studied in the impact tests to find out if the energy input had any effect on the failure mode and the failure stress. The three energy levels were introduced by dropping the impact hammer from three different drop-heights.

The slowest impact loading rate was equivalent to a minimum drop-height for which the beam 'just failed'. This low drop-height was determined to be 50 mm, which gave a failure time of approximately 30 msec and an impacting velocity of

0.9 m/sec. The velocity at impact was calculated by using the two basic expressions for potential and kinetic energy.

Two more drop-heights were used which had significantly higher energy input. At high drop-heights the specimen were 'flying' around dangerously in the laboratory after the impact failures, because of the low weight of the specimen compared to the impact hammer. This physical safety consideration determined the upper limit of the drop-height and was set at 300 mm, which resulted in a failure time of approximately 10 msec and an impacting velocity of 2.3 m/sec. This implied that the expected lowest impulse duration ratio might be as low as 1.5-2.0. For the impact tests 150 mm was chosen as the intermediate drop-height, which gave a failure time of approximately 20 msec and an impacting velocity of 1.6 m/sec. The energy input for the medium drop-height and the high drop-height was computed to be three and six times higher respectively than that for the low drop-height by using the basic expression of potential energy.

3.5 Sampling Rates

As mentioned above the analog signal was tranferred through a low pass filter of 482 Hz before it reached the digital signal processing analyser in the static set-up. It is often easier to represent an electronic component in terms of rise time rather than frequency response. Rise time of an electronic component is defined as the time required for a signal to increase from 10 % to 90 % of full amplitude. The relationship between signal frequency (f) and rise time (T_R) for a sine wave is $T_R \approx 0.35/f$. For other wave forms the constant 0.35 may vary between 0.34 and 0.39 (Ireland, 1974).

For brittle fracture, test data is considered acceptable if the failure time (t_F) is greater than the rise time (T_R) but otherwise the data is considered suspect because of excessive attenuation. The rise time (T_R) was 0.726 msec for this low pass filter.

Thus the same low pass filter from the static tests was sufficient even for the shortest expected failure times of 10-15 msec for the impact loadcell.

The sampling theorem for signal processing says that 'a continuous signal which contains no significant frequency components above f hertz may in principle be recovered from its sampled version if the sampling interval is less then 1/2f seconds' (Lynn, 1989). Appendix C describes the detailed derivation of the sampling rates for the static tests, and also gives the sampling rates for the three static loading rates.

For the impact tests 0.2 msec was used as the sampling increment which yielded a sampling rate of 5000 Hz. The sampling rate for the impact tests was determined by the limitations of the accelerometers used in some of the impact tests.

3.6 Specimen

The impact drop-weight machine resticted the maximum testing span which could practically be used without major rearrangements. When choosing the specimen size it was decided to use the largest span to depth ratio possible and to use a commercially available cross section. All the specimen had a cross section of (38 x 89 mm) and a total length of 1145 mm. An overhang of 25 mm at each support gave a clear span of 1095 mm. The span to depth ratio became 12.3 and should be compared to the standard static testing span to depth ratio of 17 (ASTM, 1989). Figure 3.11 is a sketch of the specimen dimensions and the support arrangements.

Recommendations regarding the span to depth ratio states that a ratio less than 5 yields a high percentage of shear failures and a ratio greater than 12 is intended only for evaluation of the deflection due to the bending moment. For the evaluation of flexure properties the span to depth ratio should be between 5 and 12 (ASTM, 1989). As the span to depth ratio gets closer to 5 the number of shear failures would be expected to increase.

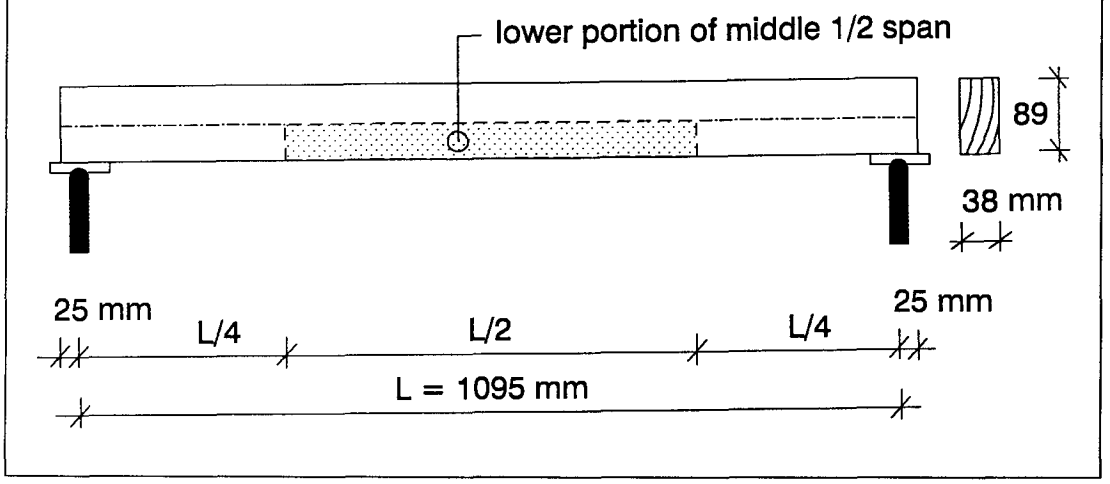

Figure 3.11: Dimensions of test specimen with hatched area.

From previously machine stress rated (2100f/1.8E and 1650f/1.5E) kiln-dried lumber, the 'clearest' pieces were manually picked out at the truss plant of Pacific Truss in Langley, BC, Canada. Typically two specimen were cut from each 3.65 m long spruce-pine-fir (SPF) graded piece of lumber. Measurements of the moisture content and the cross sectional dimensions were taken for each specimen. These were then sorted into two main material categories designated as 'class 1' and 'class 2'.

The intention with the 'class 1' material was to isolate and especially study whether the previously experienced failure mode still appeared when the indentation and penetration problems from earlier tests were eliminated. The 'class 1' material was specimens that were as much as possible the clearest wood material that could be achieved with the chosen specimen dimensions. The failure mode experienced earlier was a crack propagating more or less straight up from the bottom of the beam to its top. The intention with the 'class 2' material was to study whether the failure modes and the failure stresses changed for specimens which were more closely related to the commercially available lumber.

A specimen was classified as 'class 1' material when there were no large knots (> 10 mm), no slope of grain indications and no other indication of weakness in the lower portion of the middle half span. The 'class 2' material was divided into four different sub-groups, which are described in more detail in Appendix C.

Each specimen was marked with a codename and was stored in the Structural Laboratory until the tests were performed.

3.7 Sample Sizes

The estimate for the sample size was based on a two-sided statistical test that is presented in Appendix C. A sample size of approximately 30 was assumed to give reasonable statistical confidence for the average failure stress value, and a sample size of 60 would also give reasonable statistical confidence for the lower quartile (25th percentile), or the weaker end of the failure stress distribution. All of the groups had an original sample size of 31, except the 'class 1' material impact groups, which had a sample size of 62. Table 3.1 lists the sample sizes of the different loading rates. The notation 'no. of spec.' refers to the number of specimen for each loading rate. The notations 'dcont' and 'lcont' are associated with deformation controlled static tests and load controlled static tests respectively. Impact tests are called 'impact'. Times relate to expected failure times.

Typically three specimens of each impact test groups were videotaped and on each of these specimen there were three accelerometers mounted on top of the specimen. Another three specimens of the 'class 1' material impact test groups were tested with only three accelerometers mounted on top of the specimen. Accelerometers were mounted on a group of 27 randomly selected specimens. This group were used for the comparison of various failure stress analyses.

Table 3.1: Sample sizes of each loading rate.

loading rate	class 1 no. of spec.	class 2 no. of spec.
dcont 60 sec	31	31
dcont 3.5 sec	31	31
dcont 0.2 sec	31	31
lcont 60 sec	31	31
lcont 3.5 sec	31	31
lcont 0.2 sec	31	31
impact 30 msec	62	31
impact 20 msec	62	31
impact 10 msec	62	31
total = 651	372	279

3.8 Grouping

The modulus of elasticity was assumed to represent the strength distribution of the test material. All of the specimens were non-destructively tested in the static test set-up, and the modulus of elasticity was computed for each specimen. The specimens for each category were ranked and randomly grouped according to the modulus of elasticity into the nine different loading rates. The 'class 2' material was grouped in such a manner that each group contained the same number of specimens from each of the different sub-groups. Before the modulus of elasticity tests were performed, measurements were taken of the moisture content and of the cross sectional dimensions for each specimen.

3.9 Failure Mode Records

Records were kept of the initial failure stage for all of the specimens. Black and white photographs were taken, with an ordinary camera, of all specimen to document the different failure modes.

A few interesting and typical failure modes, or more correctly failure surfaces, were studied with an optical microscope, Olympus Vanox-S AH-2. A camera could be mounted on the optical microscope. The microscope was available in the Department of Microbiology at UBC. Black and white photographs were taken with a magnification of 40x.

Some of the impact tests were videotaped with a high speed motion camera at a rate of 1000 frames per second. The high speed motion camera and analyser was a Kodak EktraPro 1000 and was purchased from Photonic Analysis Ltd., Ont., Canada.

3.10 Summary

The static tests were performed, both load controlled and deformation controlled, using a MTS test machine. The impact tests were performed with a drop-weight impact machine designed and built at UBC. Three loading rates were conducted for each of the static loading and for the impact loading.

The indentation and penetration problem from earlier impact tests were solved by placing a steel plate between the loading head and the specimen. Steel plates were also mounted on the supports to prevent indentation and to allow rotation of the beam at its supports. The contact force between the loading head and the specimen was measured by a loadcell and was assumed to represent the load experienced by the beam.

The static data were filtered through an analog low-pass filter of 482 Hz. The impact data were collected raw and digital filtering was performed later.

A total of 651 specimens (38 x 89 x 1145 mm) were sorted into two material categories: 'class 1' and 'class 2'. The specimen were then grouped into the nine loading rates according to the modulus of elasticity obtained from non-destructive bending tests. All of the groups had an original sample size of 31, except the 'class 1'

material impact groups, which had a sample size of 62.

The failure modes were recorded with black and white photographs of all the specimen. A few specimen were studied under an optical microscope. A high speed motion camera was used to document some of the impact tests.

Chapter 4

Data Analysis

4.1 Introduction

This chapter presents the data collected during various tests and demonstrates how the data were analysed. Basic properties, such as sectional dimensions, moisture content and specific gravity are given at the beginning of this chapter. The calculated values of the modulus of elasticity are presented before the damping analysis and the stress wave analysis. The chapter ends with the failure data analysis in which the recorded data were converted to failure data suitable for the later failure stress analysis.

4.2 Sectional Dimensions

The width and depth of the specimens were measured at the midspan with a digital gauge, with an accuracy of 0.1 mm, before the modulus of elasticity tests were conducted. In Table 4.1 the mean values of the cross sectional dimensions are tabulated for each loading rate. The notation 'no. of spec.' refers to the number of failed specimens with reliable results. The notations 'dcont' and 'lcont' are associated with deformation controlled static tests and load controlled static tests respectively. Impact tests are called 'impact'. Times relate to expected failure times.The coefficients of variation were 0.01-0.02.

Table 4.1: Mean values of sectional dimensions for each loading rate.

loading rate	class 1			class 2		
	no. of spec.	width mm	depth mm	no. of spec.	width mm	depth mm
dcont 60 sec	30	38.4	88.5	31	38.5	88.0
dcont 3.5 sec	31	38.3	88.3	31	38.3	88.0
dcont 0.2 sec	31	38.4	88.5	31	38.3	88.2
lcont 60 sec	29	38.3	88.5	31	38.2	88.1
lcont 3.5 sec	31	38.3	88.2	31	38.3	88.0
lcont 0.2 sec	31	38.3	88.3	31	38.3	88.2
impact 30 msec	21	38.4	88.3	16	38.4	88.4
impact 20 msec	58	38.2	88.4	31	38.2	88.0
impact 10 msec	61	38.3	88.5	30	38.3	88.2

4.3 Moisture Content

The moisture content was measured with a Delmholst resistance moisture meter. The dial readings were converted to moisture content in percentage according to a conversion table for the specific moisture meter. The moisture content was found to be approximately 19 % for all the specimens. This was considered too high for performing the failure tests but sufficient to carry out the modulus of elasticity tests, the results of which were used to form the loading groups. The specimens were then left in the Structural Laboratory for about two months. During that time the moisture content was monitored on 31 randomly chosen specimen. The average moisture content of the randomly chosen specimen was reduced to approximately 12% after two months. The test material was then considered to be dry enough and the failure tests were performed.

4.4 Specific Gravity

Specific gravity or density was calculated from a randomly selected sample of 20 specimens which were weighed and measured after the specimens were stored for two months. The average value of the density was found to be 480 kg/m^3 and the coefficient of variation 0.09. The density value was slightly high compared to a rough estimate of the density of SPF graded lumber which was 440 kg/m^3.

4.5 Modulus of Elasticity

The modulus of elasticity tests were conducted in the static test set-up with a constant deformation rate of 0.25 mm/sec. All the specimen were loaded in the same direction in which they were later tested to failure. The specimen were loaded to 4-5 mm mid-point displacement and the mid-point load and displacement were measured. This load corresponded roughly to a stress level that was half of the 5 % failure stress for SPF SS grade (38 x 89 mm). No indications of failure initiation were observed.

A computer program was written that provided a linear regression analysis, according to the least-square method, on the relationship between the mid-point load and mid-point displacement. This relationship is the same as the slope of the load-deformation curve. The middle 70 % of the load-deformation curve was used for the linear regression analysis. The modulus of elasticity was then computed for each specimen with Equation 2.1. The measured cross sectional dimensions were used in these calculations.

The average values or mean values of the modulus of elasticity are given in Table 4.2 for both 'class 1' and 'class 2' material. The mean value was calculated on the failed specimens. The coefficients of variation were 0.10-0.12.

Table 4.2: Mean values of modulus of elasticity for each loading rate.

loading rate	class 1 MPa	class 2 MPa
dcont 60 sec	8903	8683
dcont 3.5 sec	8871	8691
dcont 0.2 sec	8866	8671
lcont 60 sec	8824	8693
lcont 3.5 sec	8911	8753
lcont 0.2 sec	8865	8587
impact 30 msec	8589	8539
impact 20 msec	8912	8485
impact 10 msec	8892	8832

4.6 Frequency and Damping

The fundamental or natural frequency and the fundamental or natural period for all the specimen were calculated to be in the range from 122 to 165 Hz and from 6.1 to 8.2 msec respectively for the given beam dimension by using Equation 2.16.

The displacement of the accelerometer was calculated by performing a double integration of the acceleration record after the initial 20 msec. It was observed that the beams vibrate with an approximate period of 7 msec, which corresponded well with the calculated fundamental period of the beams.

Damping is usually negligible in fast loading, but in this investigation the static tests do not qualify as rapid tests. The actual damping, which is the percentage of vibration that is damped out in a free-vibration situation, was experimentally determined.

The beam was struck with an ordinary hammer at one quarter of the span away from one support and the acceleration was recorded by an accelerometer at one quarter of the span from the other support. The beam was held down at the supports to avoid vertical movement at the supports, but the beam was allowed to rotate at its supports. From the data record it was possible to determine that during the initial 20 msec the

vibration of the beam was influenced by the contact between the hammer and the beam.

From three experiments performed the damping ratio was found to be 3-5 % by using the Equation 2.9. This very low damping had no significant effect on the natural frequency of the beam. Therefore damping was considered to be negligible. In other words, the dynamic system was considered to be undamped.

4.7 Stress Wave Analysis

The compression stress wave travels a certain distance in a certain time. A very rough estimate, using the first equation of Equation 2.3, gives a time of approximately 0.2 msec for the longitudinal stress wave to propagate from the loading point to the beam supports. The sampling rate for the impact tests was 0.2 msec and it would therefore have been impossible to detect any stress wave propagation. The applied load was considered to be transferred into stresses instantaneously throughout the beam for all loading rates.

4.8 Failure Data Analysis

This section explains how the recorded data from the two test apparatus were converted to failure data suitable for the failure stress analysis. The presented failure data includes failure time and failure load.

4.8.1 Static Failure Data

The load and displacement at the mid-point were measured for all specimens undergoing static tests. Because the sampling rate was known, the time step between

readings was therefore known and from the time step, the time to failure or the failure time was computed.

A computer program was written to make it easier to determine the failure load exactly and its corresponding failure time and failure displacement for each test. This program converted the voltage readings to kilo-newtons (load) and milli-meters (displacement) respectively according to the calibration factors. The static loadcell was found to have a noise level of approximately ± 0.01 volt (± 0.040 kN). If the difference between two sequential data points was higher than two times the positive noise level, the loadcell was considered to be triggered by its contact with the beam. The first of these two sequential load data points was set as the starting point of the loading event, and its corresponding load and displacement measurements were subtracted from all the following measurements.

The failure load was the maximum load experienced during a test. The corresponding time and displacement were defined as the failure time and the failure displacement respectively. The static failure stress was also calculated for each specimen.

For each loading group statistical analyses were performed on the failure load and the failure time. The mean value (mean) and coefficient of variation (cov) are given in Table 4.3 for 'class 1' and 'class 2' material. The percentile values were computed from the relative cumulative frequency distribution which was created by ranking the specimens according to their failure strength.

From Table 4.3 it is clear that both the failure time and the failure load were higher for the 'class 1' material than for the 'class 2' material. The dispersion of both the failure time and the failure load values were higher for the 'class 2' material than for the 'class 1' material. The failure load increased slightly with decreasing failure times.

Table 4.3: Failure times and failure loads for static tests.

loading rate	failure time class 1 mean sec	cov	class 2 mean sec	cov	failure load class 1 mean kN	cov	class 2 mean kN	cov
dcont 60 sec	62.7	0.24	45.2	0.28	13.6	0.16	11.1	0.22
dcont 3.5 sec	2.866	0.16	2.343	0.20	15.2	0.18	12.3	0.23
dcont 0.2 sec	0.125	0.14	0.104	0.21	15.4	0.18	12.3	0.30
lcont 60 sec	68.4	0.17	57.1	0.18	14.6	0.17	12.2	0.18
lcont 3.5 sec	4.149	0.21	3.410	0.24	14.7	0.20	12.3	0.25
lcont 0.2 sec	0.224	0.18	0.186	0.26	15.2	0.15	11.9	0.24

4.8.2 Impact Data Procedure

An extensive investigation was conducted of the external noise which affected the impact loadcell and how it influenced the output signal from an impact test. Two different filtering procedures were employed on all the impact loadcell test results.

4.8.2.1 Noise

Noise tests were carried out as free-fall tests. The hammer assembly was dropped as during ordinary failure tests but without a specimen at the supports. Measurements were recorded from the loadcell over time during the free-fall tests. The frequency spectrum was computed on the loadcell signal for the free-fall tests with the computer software VU-point Version 2.0, a product of S-Cubed a Division of Maxwell Laboratory Inc. in La Jolla, Calif., USA. A rectangular window was used for the Fast Fourier Transform (FFT), which was employed to compute the frequency spectrum. The free-fall noise from the loadcell was assumed to represent the external noise that would occur during all the impact tests. Figure 4.1 shows a typical example of a free-fall test and its frequency spectrum.

The frequency spectrum (0 to 2.5 kHz) clearly indicated that the significant frequencies were found at approximately 60, 180, and 300 Hz. These frequencies are all

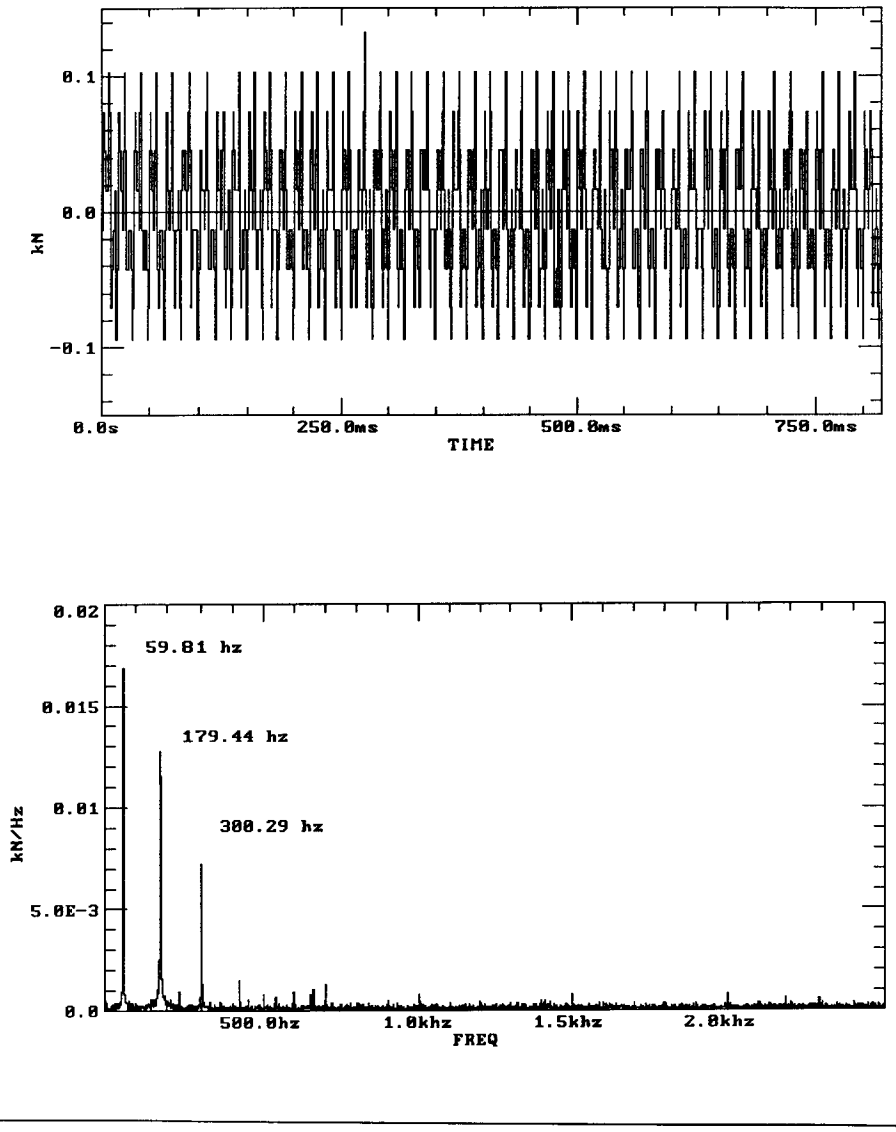

Figure 4.1: Typical free-fall test and its frequency spectrum.

multiples of the ordinary 60 Hz power line frequency.

The noise amplitude was reduced to approximately half the amplitude if a three band-reject filter was applied on the impact loadcell signal with the software VU-point. All of the digital filters employed had a frequency span of 10 Hz and were centered at the significant frequencies mentioned above. It was concluded that only the noise around the 60 Hz frequency had to be filtered away.

4.8.2.2 Filtering

Two different filtering procedures were employed on all the impact loadcell test results using the VU-point program. The first one was a band rejection filter between 55 Hz and 65 Hz. There were no significant difference between the raw signal and the band filtered signal. In the second procedure a low pass filter at 500 Hz with a transition zone of 20 Hz was employed together with the band rejection filter from the first filter procedure. This second filtering procedure had a smoothing effect on the load versus time curve.

4.8.3 Impact Failure Data

A computer program was written to correct the data for the initial voltage off-set and converted the voltage readings to kilo-newtons (load) according to the calibration factor. The sampling rate or the time step was the same for all of the impact tests. The results from the two filter procedures were ploted for all the impact tests, as illustrated in Figure 4.2. For each test the failure load was individually determined from one of the filtered curves. The failure load was determined as the maximum load experienced during a test. The corresponding time was defined as the failure time.

Statistical analysis was performed for each loading rate on the failure load and

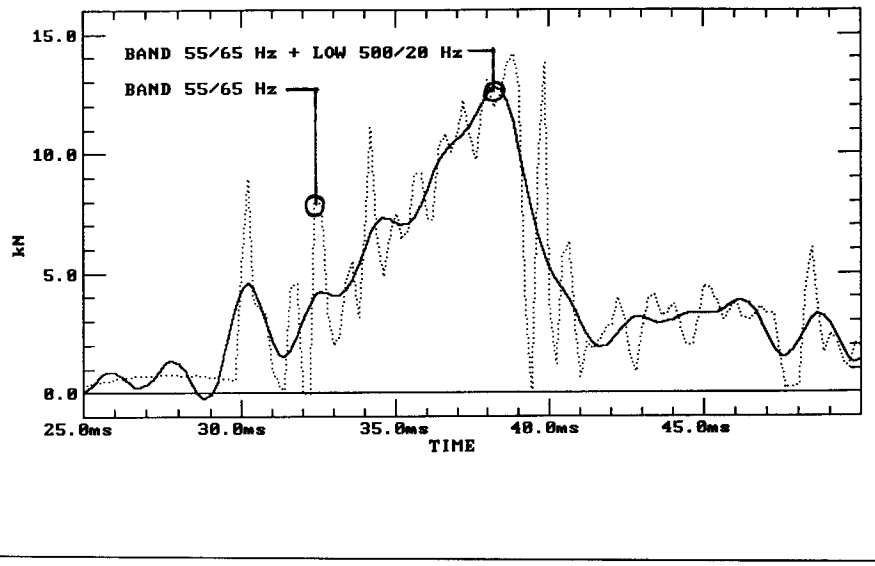

Figure 4.2: Two filter procedure for a typical impact test.

the failure time. The mean value (mean) and coefficient of variation (cov) are given in Table 4.4 for 'class 1' and 'class 2' material.

From Table 4.4 it is clear that the failure time decreased and the failure load increased slightly with increasing drop-height with the impact tests. The dispersions of the failure time values were the same for the 'class 1' material as for the 'class 2' material. The dispersion of the failure load values was higher for the 'class 2' material

Table 4.4: Failure times and failure load for filtered impact tests.

loading rate	failure time class 1 mean sec	cov	class 2 mean sec	cov	failure load class 1 mean kN	cov	class 2 mean kN	cov
impact 30 msec	0.0253	0.33	0.0245	0.26	13.5	0.16	11.9	0.21
impact 20 msec	0.0167	0.31	0.0132	0.23	16.5	0.18	12.5	0.28
impact 10 msec	0.0103	0.30	0.0090	0.30	16.0	0.22	13.8	0.33

than for the 'class 1' material. For the impact groups the average static failure stress calculated on the raw test data was 7-13 stress calculated on the filtered test data. It was concluded that the filtered data from the impact tests would be most comparable to the static test data, which were filtered through an analog low-pass filter. Therefore the filtered impact test data was used in the remaining analyses.

4.9 Summary

The sectional dimensions were measured for all the specimen. For a smaller group of specimen measurements were taken on the moisture content and the specific gravity. The modulus of elasticity was calculated for each specimen.

From damping tests the damping was considered to be negligible and therefore the dynamic system was assumed to be undamped. From stress wave analysis the stress was found to be transferred instantaneously throughout the beam for all loading rates. The failure load was determined as the maximum load experienced during a failure test. The corresponding time was defined as the failure time.

For the static tests both the failure time and the failure load were higher for 'class 1' material than for the 'class 2' material. The dispersion of both the failure time and load values were higher for the 'class 2' material than for the 'class 1' material.

An extensive investigation was conducted of the external noise which affected the impact loadcell and how it influenced the output signal from the impact test. Two filtering procedures were performed on all the test results of the impact loadcell. For each test the failure load was individually determined from one of the filtered impact loadcell curves.

The failure time and the failure load increased slightly with increasing drop-height for the impact tests. The dispersion of the failure time values was the same for the

'class 1' material as for the 'class 2' material. The dispersion of the failure load values was higher for the 'class 2' material than for the 'class 1' material. It was concluded that the filtered data from the impact tests would be most comparable to the static test data, which were filtered through an analog low-pass filter. Therefore the filtered impact test data was used in the remaining analyses.

Chapter 5

Failure Analysis

5.1 Introduction

This chapter draws conclusions from the failure stress analysis, the strength ratio analysis and the failure mode investigation. Accelerometer measurements are discussed at the beginning of the chapter. Failure data were converted to failure stress. Three different dynamic failure stress analyses are presented and they were compared to each other. Modal failure stress analysis was chosen for futher strength ratio analysis. The chapter ends with a discussion of failure modes.

5.2 Accelerometer Measurements

The comparison of the failure stress analyses was intended to be performed on the group of 27 randomly selected specimens on which accelerometers were mounted. On three of the 27 selected specimen all of the accelerometers fell off the specimen during loading. Figure 5.1 shows the locations of the three accelerometer mounted on top of the specimen. During the tests the accelerometers mounted at location 1 and 2 failed twice as often as the accelerometers at location 3. Twentynine percent of accelerometer measurements failed for accelerometers at location 3. In total, approximately 50 % of accelerometers gave useful measurements.

The high failure rate of the accelerometers resulted from failure in the glue between

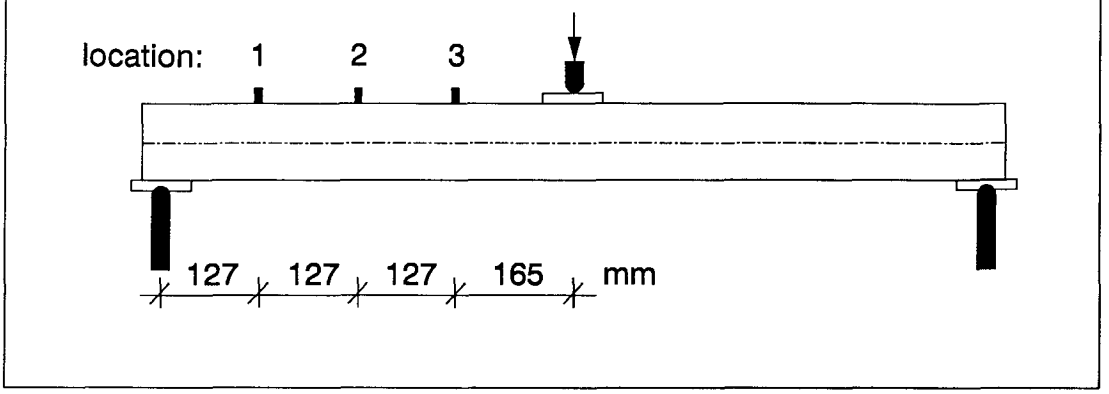

Figure 5.1: Location of accelerometers along the top of specimen.

the specimen and the base onto which the accelerometer was screwed. The glue experienced a maximum force of approximately 8 N during an impact test. This force was calculated from the maximum peak acceleration of approximately 440 kg/m^3, which was observed during tests, and the weight of the accelerometer which was 25 g. A credible explanation of the failure in the glue was that the initial impact or contact between the loading head and the beam induced some high frequency vibration. This high frequency were caused either by vibration of the steel plate between the beam and the loading head, or by vibration of the whole beam induced by the beam rocking on its supports during tests.

5.2.1 Deflected Shape of Beam

The visual impression from the slow static tests clearly indicated that the beam was deflected vertically according to the first mode of vibration. The first three modes of vibration were given in Figure 2.5 for a simple beam. If a crack was propagating from the bottom to the top of the beam it would have a higher amount of third mode of vibration and therefore deform more closely to the bi-linear distribution of

displacement. This might be the case in impact loading, and that was also one of the reasons for investigating the deflected shape of beams subjected to impact loads.

Integration of acceleration over time gave the velocity at each instant during the impact event, while double integration of the acceleration over time gave the deflection at each instant during the impact event.

The same filtering procedure was used for the accelerometer measurements as was used for loadcell measurements. A band rejection filter between 55 Hz and 65 Hz was employed together with a low pass filter at 500 Hz with a transition zone of 20 Hz. The starting value for the integrations was the same as the starting point for the loading event. Both the filtering and the double integration of the acceleration measurements were performed with the VU-point software.

From this deflected shape investigation it was not possible to determined whether the beam deflected according to a bi-linear or a sinusodial curve. This realization was explained by the sensitive and unreliable measurements from the accelerometers.

The effect of shear deformation and rotational inertia was very closely related to the shape of deflection or the mode of vibration. This effect gave an approximate 5 % increase of the natural frequency f_n for the first mode of vibration and an approximate 50 % increase for the third mode of vibration. The higher modes of vibration are scaled down in the sinusodial expression of Equation 2.31 and have therefore less influence on the total response.

5.3 Failure Stress Analysis

The three different dynamic failure stress analyses are discussed in this section. A comparison was also made between the different analyses.

5.3.1 Earlier Analysis

The earlier analysis was used in earlier drop-weight impact tests at UBC and was based on the generalized inertial load assumption. It was assumed that accelerations have the same distribution along the beam as the displacements. In the generalized inertial load expression of Equation 2.26 the bi-linear acceleration assumption gave a 2 % higher value than the sinusodial acceleration assumption for the accelerometer closest to the support (location 1). For the accelerometer furthest away from the support (location 3) the sinusodial assumption gave a 15 % higher generalized load then the bi-linear assumption. The sinusodial assumption of the generalized inertial load was 4 % higher than the bi-linear assumption for the accelerometer in the middle of the specimen (location 2). It was concluded that the location of the accelerometers were very important to the reliability of the calculation of the generalized load.

The accelerometer closest to the support failed more often than the other accelerometers, while accelerometers closest to the middle of the specimen were most sensitive to the assumption of the acceleration distribution along the length of the beam. The large number of failures of measurements from the accelerometers raised serious concern about the reliability of the measurements from the accelerometers.

In the earlier analysis the initial velocity of the beam induced by the drop of the impact hammer was considered by the inclusion of the accelerometer readings into the analysis. The goal with the earlier analysis was to calculate the maximum bending load and not the failure stress.

The solution algorithm for the earlier analysis method was set up in a Lotus 1-2-3 spreadsheet from Lotus Development Corparation in Cambridge, Mass., USA. Both the bi-linear and sinusodial assumptions were used for the distribution of acceleration along the beam. The difference between these two assumptions observed on the failure stress was in the range of $\pm$ 3 % of the sinusodial assumption and was therefore

considered of no significance. In simple beam theory the beam is assumed to have a sinusodial displacement distribution. The results from the earlier analysis did not agree well with the previous conclusion regarding the sensitivity of the location of accelerometers along the beam in the calculation of the generalized load. Therefore the results from the earlier analysis was considered very unreliable. In the following comparison of failure stress analyses the sinusodial assumption of the acceleration distribution was employed for the earlier analysis.

5.3.2 FENTAB Analysis

The FENTAB analysis was performed with a finite element program in which symmetry was used. Half the length of the beam was divided into 10 finite elements, as well as 20 and 40 finite elements. The FENTAB analysis performed with 20 and 40 finite elements gave approximately 2 % higher failure stress compared to the FENTAB analysis with 10 finite elements and that difference was considered to be of no significance. In the following comparison of failure stress analyses the differentiation into 10 finite elements was employed for the FENTAB analysis. Because of symmetry the applied load was introduced with half its magnitude. The applied load was assumed to be a ramp load.

The initial velocity was introduced into the problem using three different assumptions regarding the distribution of the initial velocity. Figure 5.2 shows the three different initial velocity assumptions used in the FENTAB analysis. The distance $l/2$ of two finite elements became 52.25 mm for the 10 finite element computation. The initial velocity $\dot{v}(0)$ was introduced with the full magnitude. The first assumption, Figure 5.2 (a), was a point velocity at the line of symmetry. The distribution between node 10 and node 11 were given by a shape function defined in the FENTAB program. The second assumption, Figure 5.2 (b), was a linear velocity distribution

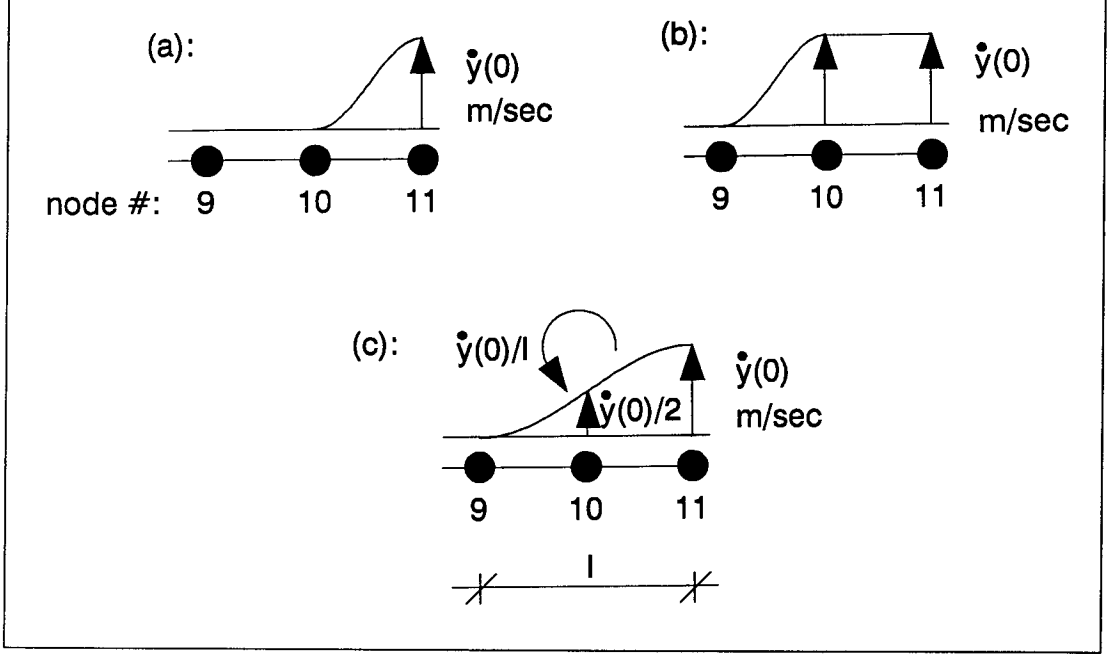

Figure 5.2: Three initial velocity assumptions for the FENTAB analysis.

over the two most central finite elements. The third assumption, Figure 5.2 (*c*), was a smoother velocity distribution over the two most central finite element.

The FENTAB computer program supplied the strain at the top and bottom end of the cross section at the middle of the length of each finite element. The distribution of the strain along the beam was found to be bi-linear which corresponds with Hooke's law. The strain at the midspan of the beam was therefore linearly extrapolated from the values of strain at the middle of the length of each finite element.

The difference in computed failure stress between the three velocities was negligible because the difference in initial velocity assumptions were less than 1 %. As expected, the failure stress from the third assumption of initial velocity, Figure 5.2, gave a stress value which fell in between those from the two other velocity assumptions. The third assumption of initial velocity was used in the following comparison of failure

stress analyses because it was most realisicly represented the distribution of the initial velocity transferred through the steel plate to the specimen.

The FENTAB analysis employed a very detailed finite element program which required relative to the other failure stress analyses a longer computation time. Therefore the FENTAB analysis implied an inefficient use of the finite element program for this investigation.

5.3.3 Modal Analysis

The modal analysis was a mode-superposition analysis of a distributed-parameter system. A close form solution of the simple beam equation was obtained for a ramp load assumption with an initial velocity at the point of impact and was given in Equation 2.33. The software MathCAD from Addison-Wesley Publishing Company Inc. in Reading, Mass., USA, was employed to perform the calculations for the modal analysis, in which the failure data from the tests were converted to failure stresses. The software is described as an electronic scratchpad for calculation and analysis. Appendix D is a copy of the output from one of the MathCAD calculations performed on one of the loading rates.

In the expression for the dynamic stress, Equation 2.33, the mode number in the denominator is only to the second order, as compared to the fourth order in the expression for the dynamic displacement, Equation 2.31. This implied that more modes of vibration had to be included in the modal analysis to represent the stresses with an acceptable degree of accuracy than was required to represent displacements. Convergence of the failure stress or failure moment was assumed to have been reached by using 47 terms in the sinusodial series expression of the total dynamic moment. In the failure stress expression 23 out of the 47 terms were zero. If 47 terms were used for the sinusodial series expression of the static moment then 99.7 % of the static

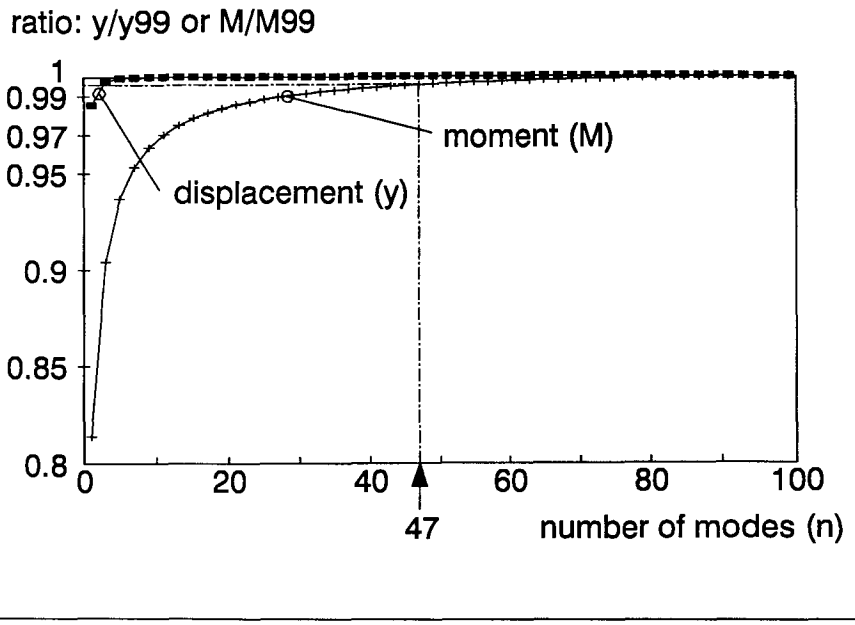

Figure 5.3: Number of modes for convergence.

moment would be captured. If 11 terms were used in the failure stress expression the average failure stress value became 2-4 % lower than the average failure stress value computed with 47 terms. It was concluded that 47 terms would represent the failure stress with more accurancy then 11 terms would do. The 47 terms (out of which 23 are zero) expression of the failure stress was used in the remaining analyses.

The convergence of the displacement expression and the moment expression is illustrated in Figure 5.3 where displacement ratio and moment ratio are plotted against the number of modes. Number of modes corresponded to the number of terms.

In the modal analysis the solution was divided into its static and dynamic parts. The impact tests indicated that the impact loading could be modelled as a ramp load. The difference between the static analysis and the static solution part from the modal analysis was less than 1 % and was considered to be of no significance.

5.3.4 Comparison of Failure Stress Analyses

In Figure 5.4 the failure stresses from the three different analyses are presented for the 'class 1' material and the 'class 2' material, respectively, that were used in this comparison study. The static part of the modal analysis is also provided in Figure 5.4. The specimens are ranked according to the modal dynamic failure stress. The comparison of failure stresses was conducted on a total of 24 randomly selected specimens.

The failure stress from the earlier analysis did not show any consistency compared to the other analyses. The main reason to abandon the earlier analysis in this investigation was the unreliable measurements of the accelerometers.

The two modal solution parts and the FENTAB solution were consistently ranked close to each other for almost all of the specimens studied. The failure stress values from the FENTAB analysis was between the static and dynamic failure stress values as calculated by the modal analysis. The FENTAB analysis was the most flexible analysis and was a very detailed analysis, but was, relatively to the modal analysis, more inefficient in this investigation and therefore more time consuming to perform. It was concluded that the capacity of the FENTAB analysis went beyond the objectives of this thesis and was therefore abandoned.

The modal static failure stresses were higher than the modal dynamic failure stresses for the weaker specimens, but this was reversed for the stronger specimens. This suggested that the failure stresses might be decreased by the inertia effect for the weaker specimens and that the failure stresses might be increased by the inertia effect for the stronger specimens. This difference in failure stress was strongly believed to be caused by differences in failure modes.

The modal analysis was a more direct and faster analysis which fulfilled the objectives of this thesis and was therefore used for the remaining analysis procedure.

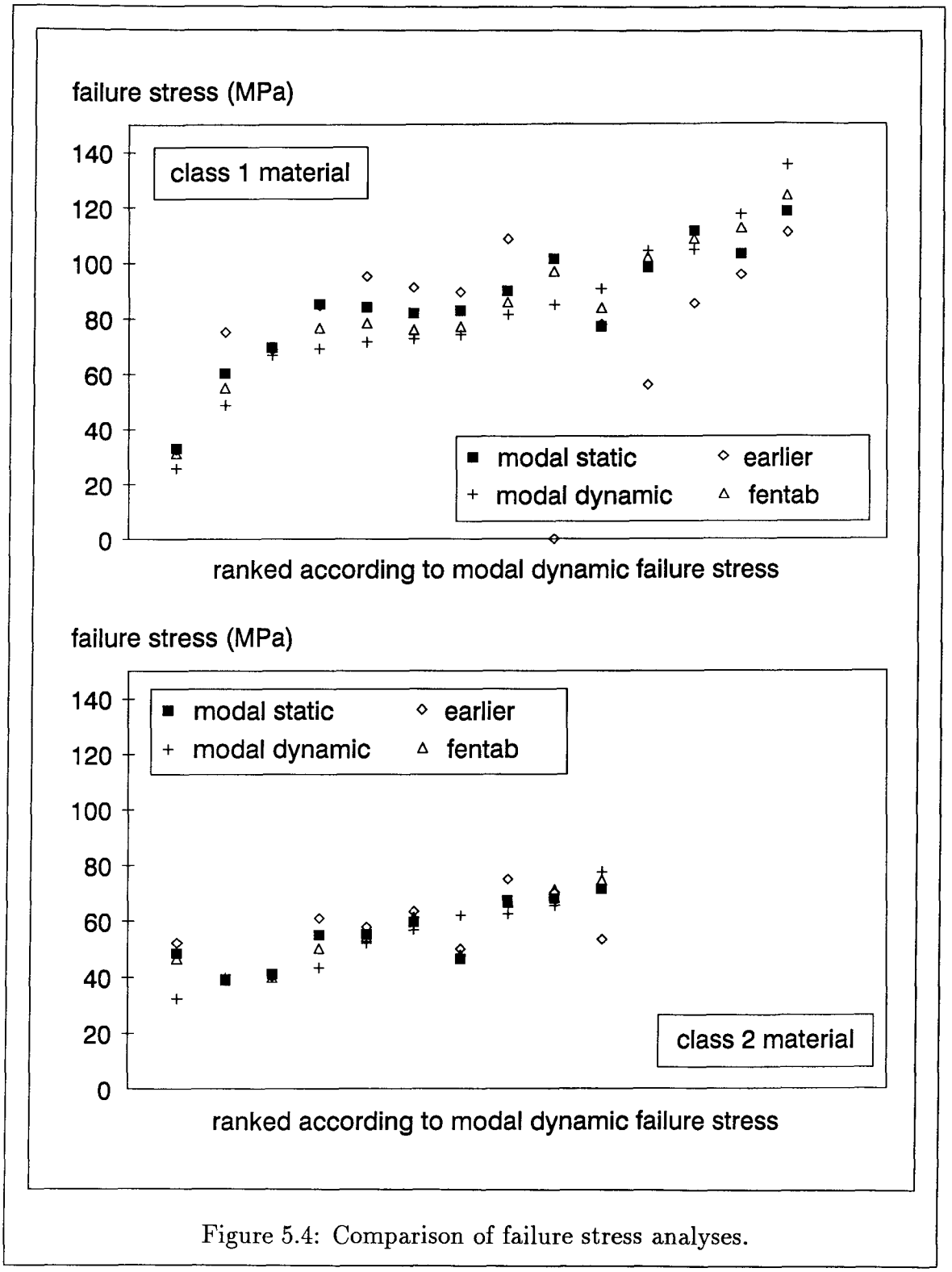

Figure 5.4: Comparison of failure stress analyses.

5.4 Strength Ratio Analysis

All the computations in this section were based on failure stress values from the modal analysis. The traditional duration of load theory and the strength ratio theory were used in an attempt to bridge the gap between static and impact loading. These approaches are presented in the section about duration of load analysis. The distribution of the strength ratio from the different impact loading groups was compared with the theoretical response ratio expression for a ramp load. At the end of this section the non-parametric percentile values of the strength ratio based on the distribution of dynamic failure stresses were compared to the non-parametric percentile values of the strength ratio based on the distribution of strength ratios.

5.4.1 Duration of Load Analysis

The duration of load analysis were performed in three ways. The non-parametric 25th and 50th percentiles of the strength ratio were found by using the distribution of dynamic failure stress. The three duration of load analyses, which are investigated in this section, are schematicly explained in Figure 5.5.

The first approach was based on the traditional duration of loading theory and was called the duration of load approach. The duration of load approach was conducted on both the static and dynamic failure stresses. The failure stress values from each different loading rate were related to a standard short term failure stress value. The standard short term loading was, in this thesis, considered to be the load controlled loading rate with a failure time of approximately 60 seconds.

The second approach was based on the strength ratio theory and was called the modal strength ratio approach. The modal strength ratio was defined as the ratio between the dynamic failure stress value and the static failure stress value from each

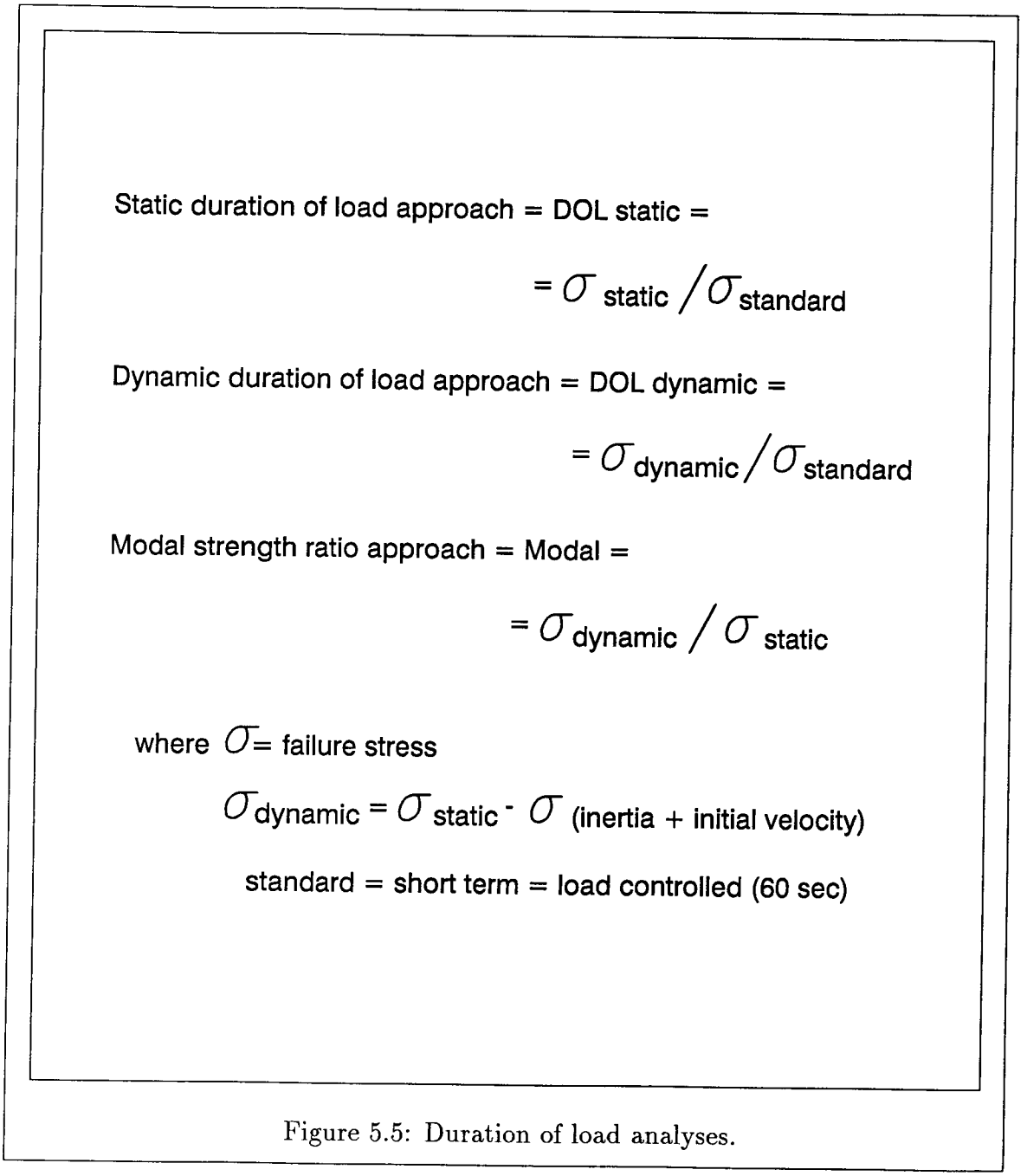

Figure 5.5: Duration of load analyses.

individual test specimen.

Figure 5.6 and Figure 5.7 show the results for the different strength ratio calculations for the 'class 1' material and 'class 2' material respectively. The indications 'DOL static' and 'DOL dynamic' state that the duration of load approach was performed on static failure stress values and dynamic failure stress values respectively for the modal analysis. The indication 'Modal' stands for the modal strength ratio. The average failure times were used on the time axis and written above the arrows for each of the loading rates.

The differences in failure strength between the deformation controlled tests and the load controlled tests were less than 18 % for all the loading rates. The mean value of the strength ratio and the failure time were calculated for these two static tests and the static tests are denoted 'static' in Figure 5.6 and Figure 5.7. The impact tests are denoted 'impact' in the same graphs.

Overall the 'class 1' material had higher failure strengths than the 'class 2' material. The 'class 2' material showed overall a larger variation or spread of the failure strength then the 'class 1' material. Lower strength values were experienced for some of the deformation controlled static tests as compared to the load controlled static tests. In this investigation the failure strength level was overall higher than the failure strength level in the earlier investigation concerning the load application (Mindess and Madsen, 1986) and this was the reason why the findings from the two investigation contradict each other.

The non-parametric 25th and 50th percentile values for the 'class 1' and 'class 2' material form the four material groups. The importance of proper or appropriate duration of load analysis is clearly demonstrated in the way the results of the three duration of load analyses are differentiated for the four material groups. The general tendency was that the 25th percentiles had smaller strength ratio values than the

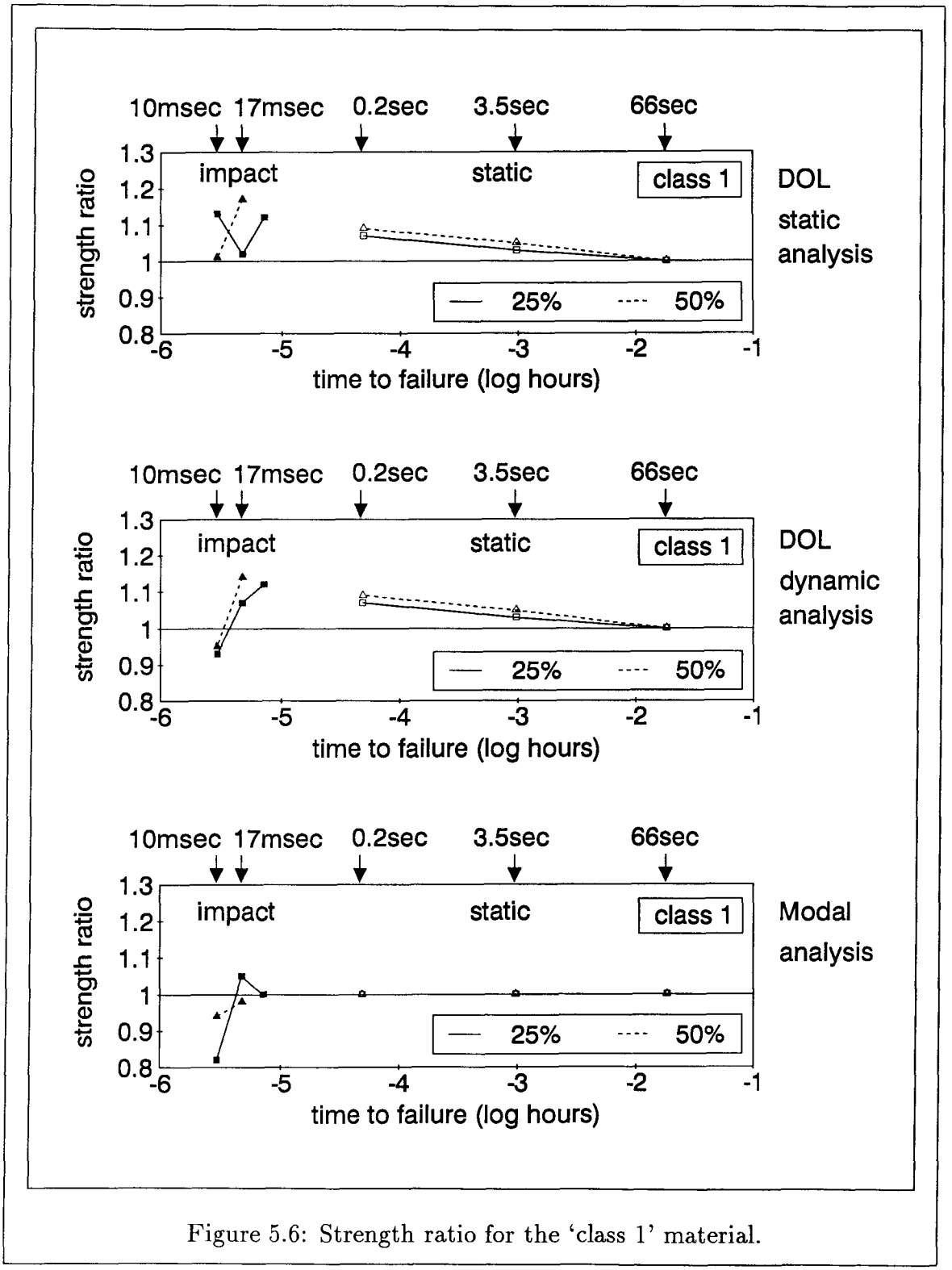

Figure 5.6: Strength ratio for the 'class 1' material.

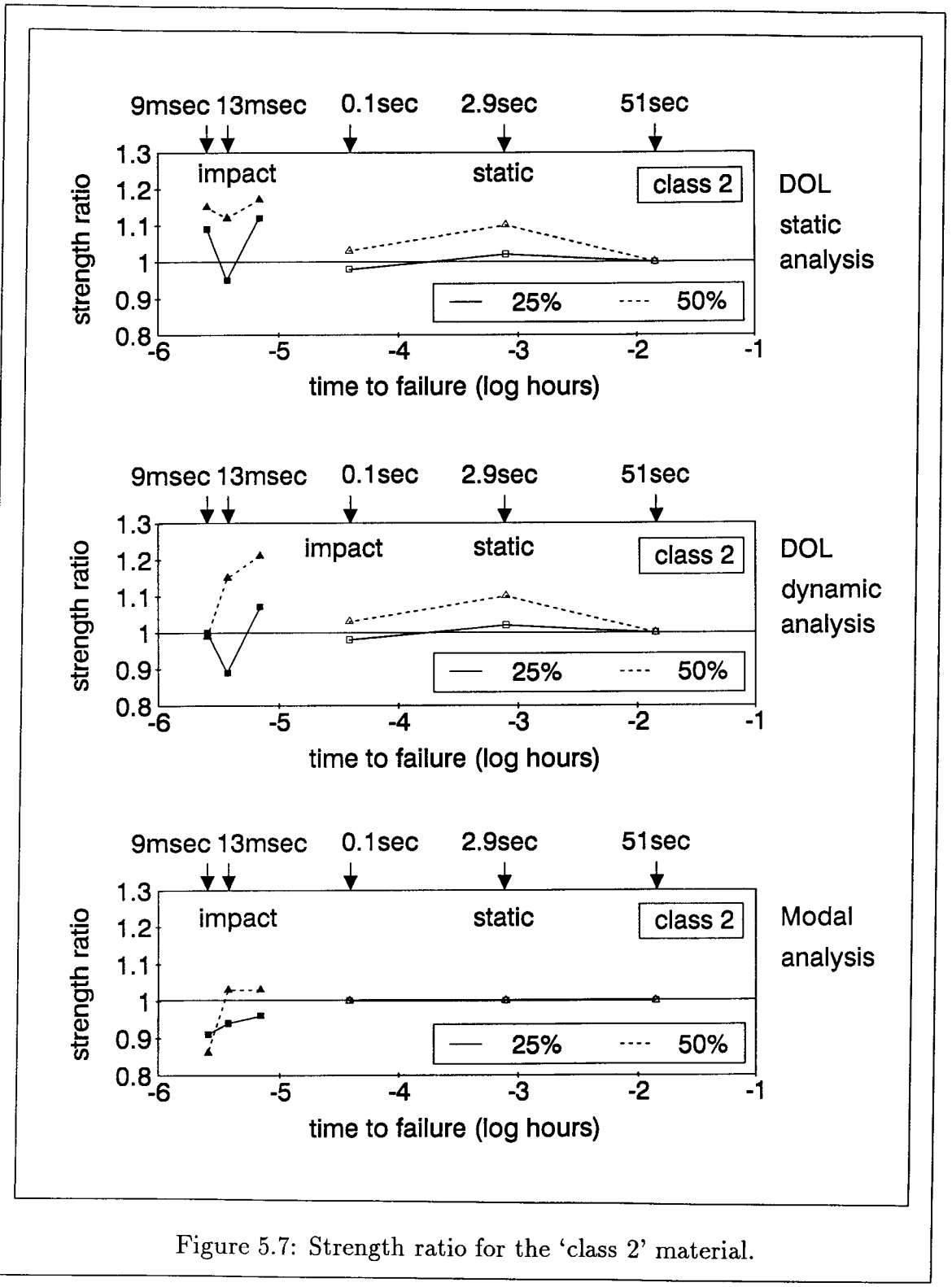

Figure 5.7: Strength ratio for the 'class 2' material.

50th percentiles.

The general tendency for the static duration of load approach was that the failure stress increased with decreasing failure time. The static duration of load ratio is a very deceptive indication of the true failure stress of the material. The inertia effect of the beam and the time-history of the load have to be taken into consideration in the duration of load approach if the strength ratio is calculated with the dynamic failure stress.

It is incorrect to rely on a specific value, such as the standard slow term failure stress. The general tendency for the dynamic duration of load approach was that the failure strength increased with decreasing failure time. The 50th percentile of the 'class 2' material was a clear exception from that general tendency, and showed an increase in the failure strength instead.

The modal strength ratio approach showed smaller variations in the strength ratio than the duration of load approach. From the modal strength ratio it was concluded that there was no difference in strength among the different static tests. The general tendency for the modal strength ratio approach was that the failure strength decreased with decreasing failure time. The only exceptions were the 25th percentile of the 'class 1' material subjected to impact tests with 150 mm drop-height and the 50th percentiles of the 'class 2' material subjected to 50 mm drop-height and 150 mm drop-height. For these particular cases a minor increase of the failure strength was experienced.

If the duration of load approach was employed for relatively small sample sizes, as in these tests, the variation or spread between the various groups was assumed to have an effect on the calculated strength ratio. For a material such as wood or timber a large number of specimen have to be used to form groups in order to achieve perfectly matched groups. The modal strength ratio approach takes the variation between the

various groups into account because the modal strength ratio was computed directly for each specimen.

A dynamic analysis approach considers the energy input induced by the impact loading and the inertial forces occuring during impact loading. A static analysis approach does not account for these very important aspects of impact loading and it is simply wrong to neglect the inertia forces in this type of loading. It was concluded that the modal strength ratio approach was more appropriate than the duration of load approach in fast rate of loading tests such as impact loading.

5.4.2 Strength Ratio Distribution

The sensitivity of the impulse duration ratio was investigated with regard to the modal strength ratio.

In Figure 5.8 and Figure 5.9 the modal strength ratio and the theory response ratio are plotted against the impulse duration ratio for each specimen of the 'class 1' and 'class 2' material respectively. Each figure contains three graphs, one for each of the impact drop-heights. The designation 'test specimens' stands for the modal strength ratio and is marked for each specimen, and the designation 'theoretical' stands for the theoretical response ratio and is marked with a solid line. Each of the impact loading groups are denoted with 'class 1' or 'class 2' for material type as well as with a drop-height distance.

All of the impact groups except the highest drop-height of the 'class 2' material groups (class 2 300 mm) showed good correlation between the modal strength ratio and the theoretical response ratio. The distribution of the modal strength ratio remained within an envelope indicated by the theoretical response ratio curve. Some of the more extreme specimens among the medium and high drop-heights tests differ more from the theoretical curve than the other specimens. It should be noted that

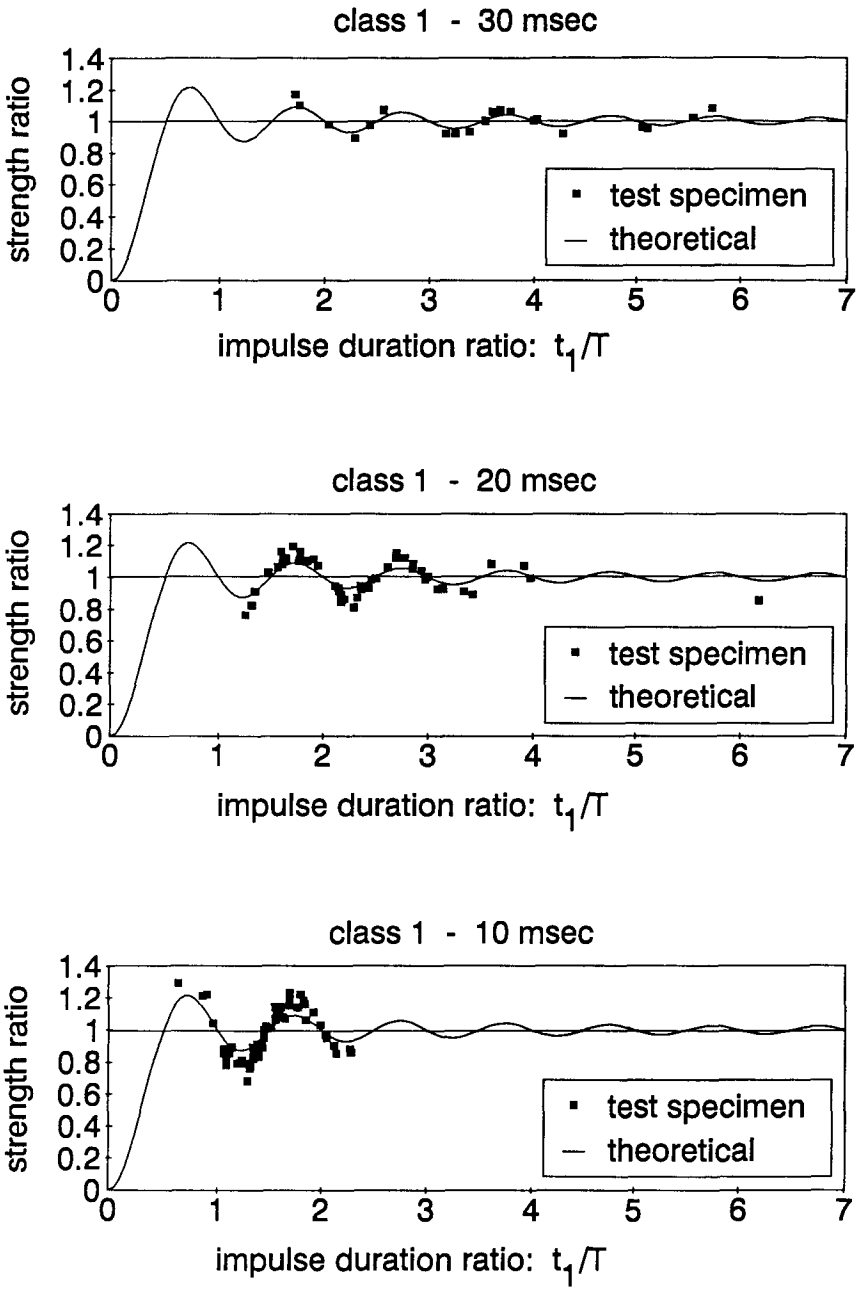

Figure 5.8: Strength ratio distribution for 'class 1' material.

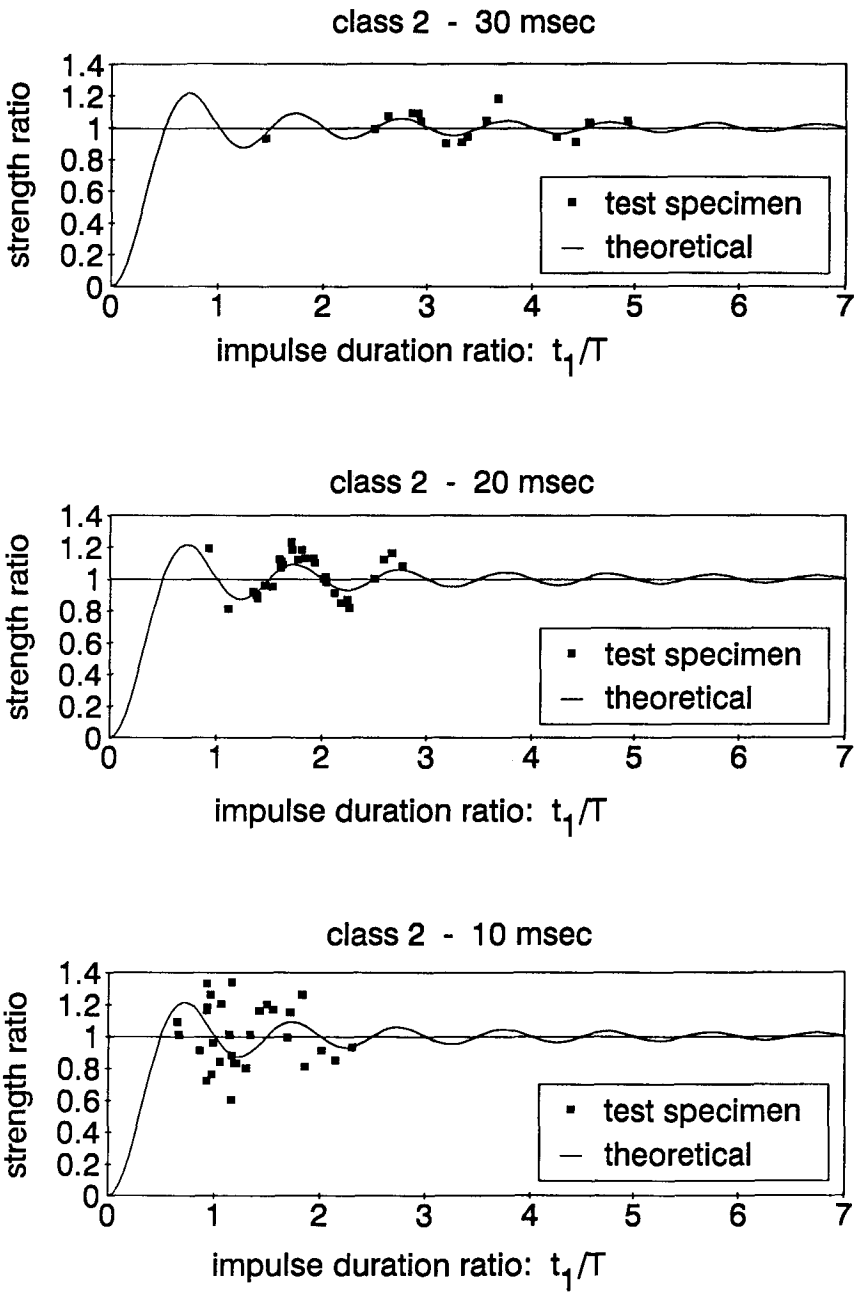

Figure 5.9: Strength ratio distribution for 'class 2' material.

the theoretical curve was created with the assumption of zero initial conditions, and that increasing drop-heights gave increasing initial velocities. It was concluded that the initial velocity had an influence on the strength ratio for the strongest specimens among the medium and higher drop-heights tests.

5.4.3 Impact Strength Ratio Analysis

It was concluded from the modal strength ratio analysis in section 5.4.1 that there was no change in the failure stress among the static test results. In section 5.4.1 the non-parametric percentiles were found on the basis of the dynamic failure strength distribution. This approach was compared to forming the non-parametric percentiles based on the ranking of the modal strength ratio distribution and this comparison is presented in this section.

The modal strength ratio percentile values based on the ranked distribution of the dynamic failure stress are plotted together with the modal strength ratio percentiles based on the ranked distribution of the modal strength ratio in Figure 5.10 for the 'class 1' and 'class 2' material respectively. The values based on the distribution of the dynamic failure stress are indicated 'stress'. The values based on the distribution of the modal strength ratio are indicated 'ratio'. The percentile values denote the non-parametric percentile strength ratio values. The dotted lines in Figure 5.10 indicate the linear regression curves computed from the percentile values based on the distribution of the modal strength ratio.

The ranking of the modal strength ratio showed a more consistant tendency of decreasing strength with decreasing failure time as compared to the ranking of the dynamic failure stress. The 25th percentile and 50th percentile strength ratios were more clearly divided for the values based on the ranking of modal strength ratio than for the values based on the dynamic failure stress. It was concluded that the ranking

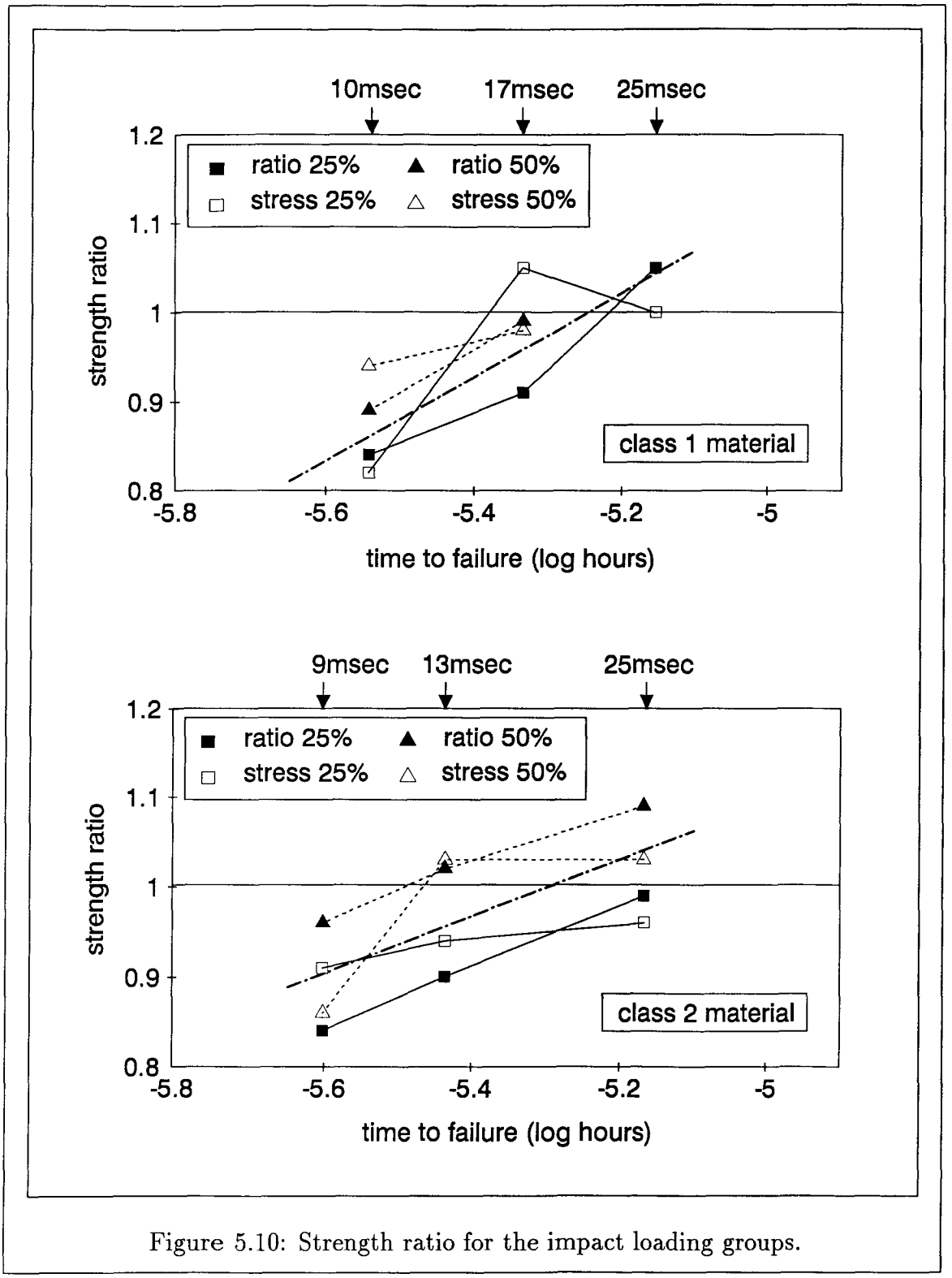

Figure 5.10: Strength ratio for the impact loading groups.

of the modal strength ratio was the most appropriate to use as base for strength ratio computations. The following conclusions were derived on the strength ratio based on the ranking of the modal strength ratio.

For both 'class 1' and 'class 2' material the strength ratio for the high drop-height (300 mm) decreased approximately 15 % at the 25th percentile. For the 50th percentile of the high drop-height the strength ratio decreased approximately 10 % for the 'class 1' material and approximately 5 % for the 'class 2' material. The decrease for the intermediate drop-height (150 mm) at the 25th percentile was approximately 10 % for the 'class 1' material and approximately 5 % for the 'class 2' material. For the strength ratio at the 50th percentile no significant change appeared for both 'class 1' and 'class 2' material for the intermediate drop-height. The results at the 50th percentile of the class 2 material were regarded as unreliable at the short drop-height (50 mm) because only 16 specimens out of 31 failed. The short drop-height did not indicate any significant change in the strength ratio for either 'class 1' or 'class 2' material.

The modal strength ratio approach offers a convenient and correct way to separate the dynamic effect of the loading type from the static strength of the specimen. The distribution of static bending strengths is taken into consideration in the design procedure by assigning strength values from standard static tests. The effect of impact loading depends on the strength ratio distribution at each drop-height. The correct approach to duration of loading problems related to impact loading is to determine the strength amplification from the ranked modal strength ratio for each of the loading rates. From the linear regression curves, the dotted lines in Figure 5.10, it was concluded that the failure strength decreased similarly for the two material categories.

It was concluded that during impact loading a strength decrease of 15 % could

be expected for the weaker specimens compared to standard short term strength. This conclusion contradicts the general belief that impact loading is associated with a strength increase, but is consistent with earlier impact tests at UBC.

5.5 Failure Mode Investigation

The description of failure modes was separated into four different initial failure modes, but was later reduced to three to make the interpretation of the failure mode data easier. A microscopic study of the failure surfaces is presented at the end of this section.

5.5.1 Failure Modes Types

The initial failure modes were defined and divided into four different failure types:

C compression initiated failure

B brash initiated failure

S slope of grain initiated failure

K knot initiated failure

Figure 5.11 schematically shows these four initial failure modes. The brash initiated failure mode was caused by tension stress parallel to grain. The compression initiated failure mode was caused by compression wrinkles which developed in the compression zone of the beam under the edges of the steel plate.

The number of initial failure modes was reduced to three in order to make the failure mode interpretation easier. All the initiations caused by some kind of knot (K) were considered to be a local slope of grain initiated failure. Both the knot initiated failure mode (K) and the slope of grain initiated failure mode (S) were caused by tension stress perpendicular to grain. These two failure modes were therefore incorparated into a new initial failure mode type called tension perpendicular to grain

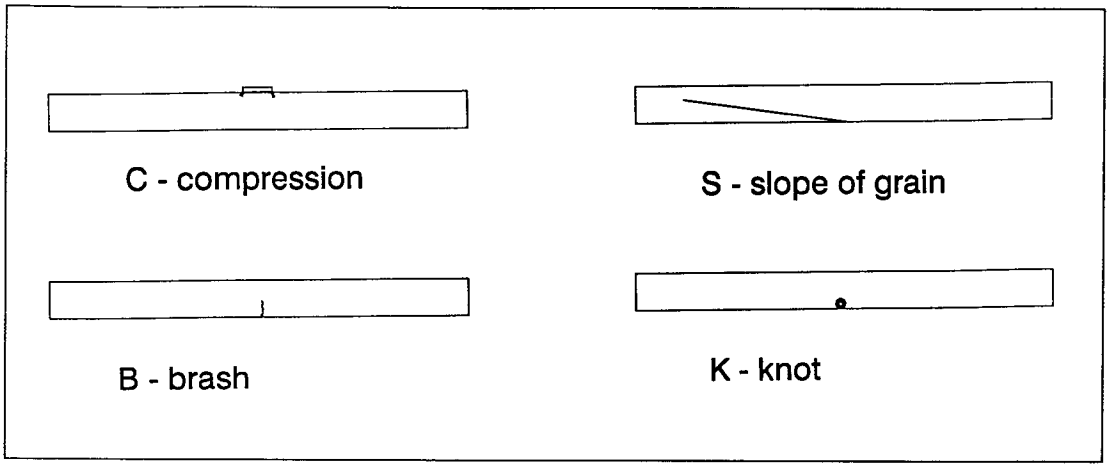

Figure 5.11: Different failure modes.

initiated failure and was denoted as TP. The clear majority of failure were initiated by a knot for the 'class 2' material.

5.5.2 Failure Mode Data

Table 5.1 presents the initial failure mode statistics for all the specimens. In Figure 5.12 the percentage of compression initiated failure modes is presented for 'class 1' material. The 'class 2' material showed a smaller portion of compression initiated failure modes than the 'class 1' material.

Deformation controlled static tests showed approximately twice the amount of compression initiated failure modes compared to load controlled static tests for the 'class 1' material. A compression initiated failure mode reduced the effective cross section, lowered the neutral axis, and decreased the moment of inertia and consequentially decreased the stiffness of the beam. The beam failed earlier with a more brash type of failure and at lower failure stress. In other words, a severe compression initiation yielded a lower failure stress provided that the tension zone of the beam was strong, as it was for 'class 1' material.

Table 5.1: Initial failure modes for all the specimen.

loading rate	class 1 no. of spec.	C %	TP %	B %	class 2 no. of spec.	C %	TP %	B %
dcont 60 sec	30	87	13	0	31	32	52	16
dcont 3.5 sec	31	52	13	35	31	6	65	29
dcont 0.2 sec	31	32	23	45	31	0	52	48
lcont 60 sec	29	45	17	38	31	0	48	52
lcont 3.5 sec	31	20	32	48	31	7	45	48
lcont 0.2 sec	31	13	45	42	31	3	71	26
impact 30 msec	21	19	57	24	16	0	56	44
impact 20 msec	58	14	34	52	31	0	55	45
impact 10 msec	61	0	57	43	30	0	40	60

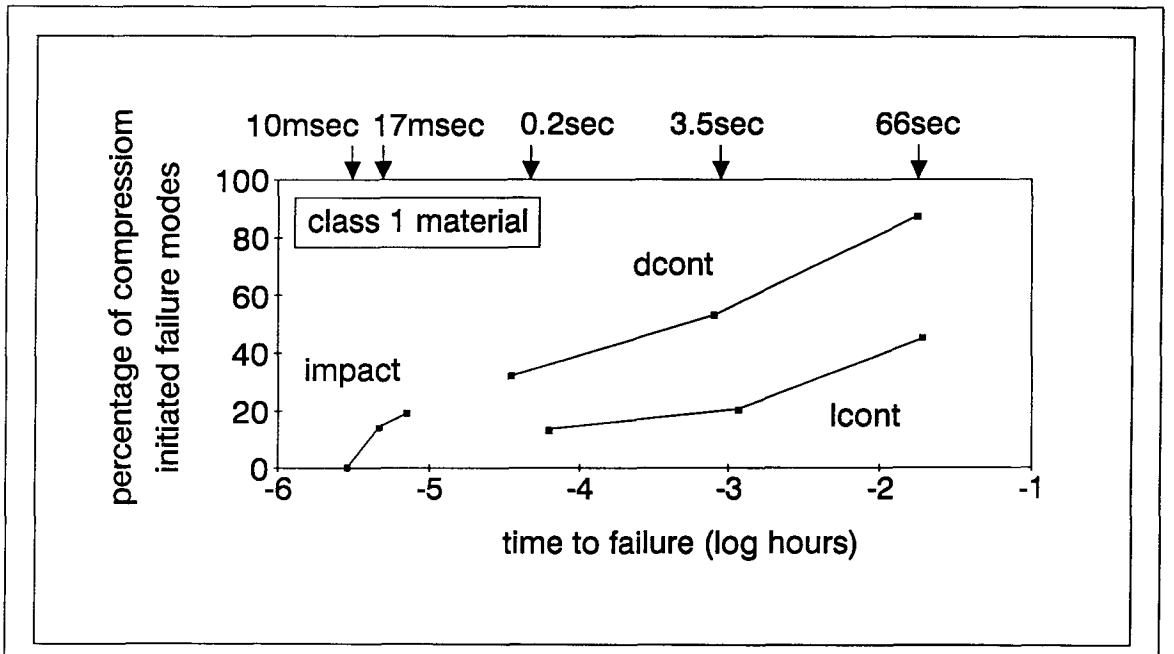

Figure 5.12: Compression initiated failure modes for 'class 1' material.

The overall tendency for both 'class 1' and 'class 2' material was that the percentage of compression initiated failures decreased with decreasing failure time.

The deformation controlled static tests showed a difference in the division between the tension perpendicular to grain initiated failure mode and the brash initiated failure modes for the 'class 1' and 'class 2' material. For 'class 1' material the percentile of brash initiated failure modes were more then 50 % higher than the percentile of tension perpendicular to grain initiated failure modes. The percentage brash initiated failure modes increased with decreasing failure time for the deformation controlled static tests. For the load controlled static tests the percentage of tension perpendicular to grain initiated failure modes increased with decreasing failure time.

There was no general tendency in the division between the tension perpendicular to grain initiated failure modes and brash initiated failure modes for the 'class 1' and 'class 2' material which were subjected to load controlled static tests. The fastest loading rate (0.2 sec) had a higher percentile of tension perpendicular to grain initiated failure modes than brash initiated failure modes. The brash initiated failure modes were more frequent than the tension perpendicular to grain initiated failure modes for the other loading rates.

The lowest drop-height (50 mm) of the impact tests of both 'class 1' and 'class 2' materials had a higher percentile of tension perpendicular to grain initiated failure modes than brash initiated failure modes. For the 'class 1' material tested at 150 mm drop-height the brash initiated failure modes were more frequent than the tension perpendicular to grain initiated failure modes, but for the 'class 1' material tested at 300 mm drop-height that effect was reversed. For 'class 2' material the division was opposite to that of the 'class 1' material for the intermediate (150 mm) and high (300 mm) drop-height of impact loading.

The high drop-height test with the 'class 2' specimens had a higher percentage

of brash initiated failure modes than tension perpendicular to grain initiated failure modes, but for 'class 1' material that effect was reversed.

5.5.3 Microscopical Study

Two failure modes or failure surfaces were found to be of major interest. The first was the tension parallel to grain initiated failure mode or the brash initiated failure mode, and was denoted 'brash'. The second was the tension perpendicular to grain initiated failure mode, and was denoted 'slope'. Four specimen were selected respectively for each of these two failure types. Two of these four were specimens tested under fast loading (impact 300 mm) and the other two were tested under slow loading (static 60 sec). For both the fast and slow loaded specimens, one specimen was taken from the strong end of the failure strength distribution and another specimen was taken from the weak end of the failure strength distribution. Figure 5.13 and Figure 5.14 are photographs of the failure surface taken through the microscope at 40 times magnification.

From the microscopical study it was not possible to draw a distinction between specimens subjected to slow loading and fast loading for either 'brash' or 'slope' failure surfaces.

The longitudinal tracheids or longitudinal cells were broken in clear tension failure for the 'brash' failed specimen, as is seen in Figure 5.13. The annual growth rings are visible as the more dense areas of cells. The location of the failure surface were probably determined by the interconnected rays between the individual cells. The interconnected rays introduced small groups of 'mini-knots' in the longitudinal direction of the cell wall.

Figure 5.14 shows the failure surface of the 'slope' failed specimen. The darker sections are the latewood and the shorter lines or hairs across the length of the

Figure 5.13: 'Brash' failure surface photographed in microscope (40x).

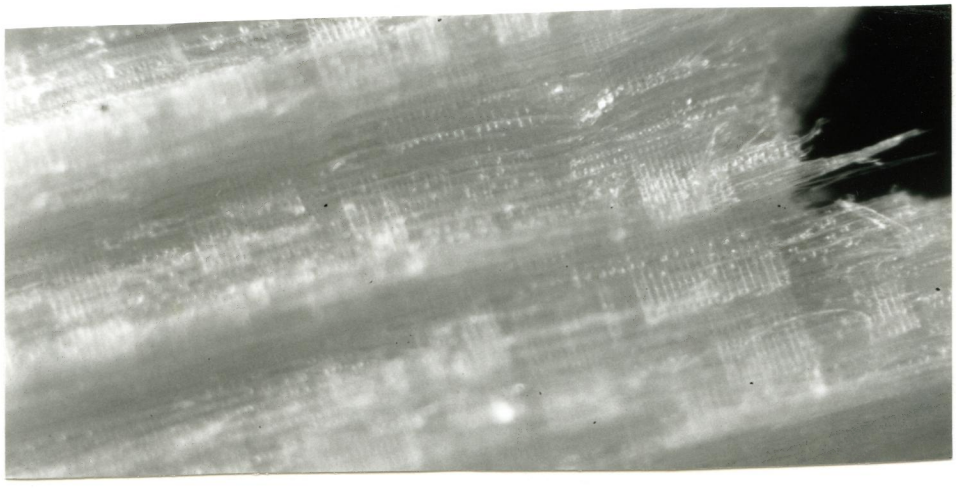

Figure 5.14: 'Slope' failure surface photographed in microscope (40x).

annual growth rings are the ray cells. The amount of visible ray cells varied within the investigated specimen, which indicated that the failure surface did not always follow the radial plane.

5.5.4 Typical Failure Modes

Studies of the fast video recording showed that the failure was very brittle and occurred within 1-2 msec after the first crack initiation was observed. The video recordings showed more 'brash' failure mode for the impact tests at the higher drop-heights. If the energy input from the impact loading was high enough the energy release from the beam during failure became too high for a tension parallel to grain failure mode and instead became a tension perpendicular to grain failure mode.

The typical failure mode for a slow loaded 'class 1' specimen was initiated by a ductile compression initiation and was followed by a brash tension failure or jagged tension failure. The 'class 1' material showed less of a compression initiation with decreasing failure time. The compression cracks needed more time to develop and therefore occurred more at the slow loading rates. It should be remembered that even a small compression failure could be devastating for the failure strength, especially if the loading direction changed, which is very likely to occur during an earthquake or other cyclic loading.

The typical failure mode for a 'class 2' specimen was initiated by a knot and was followed by a cracked failure. A cracked failure was a crack extention parallel to the grain, a jagged tension failure, a shake failure or a slope of grain failure. From the fast video recordings the failure mode for the 'class 2' specimen was less of a cracked failure mode and more of 'brash' failure mode when the failure time decreased.

Finally it was concluded that the 'class 1' material showed a failure behaviour closer to small clear specimens and the 'class 2' material showed a failure behaviour

closer to commercial lumber.

5.6 Summary

Three different dynamic failure stress analyses were applied and compared to each other. A dynamic analysis approach considered the energy input induced by the impact loading and the inertial forces occuring during impact loading.

The earlier analysis was based on the generalized inertial load assumption. The large number of failures of measurements from the acclerometers raised serious concern about the reliability of the measurements from the accelerometers. It was assumed that the distribution of acceleration along the beam was the same as the distribution of displacement along the beam. The bi-linear and sinusodial distribution of displacement assumptions were separated the most from each other in the calculations of the generalized load when the accelerometers were furthest away from the supports. The main reason to abandon the earlier analysis was the unreliable measurements of the accelerometers.

The FENTAB analysis was performed with a finite element program which was very flexible and detailed. The FENTAB analysis was, compared to the modal analysis, more inefficient and more time consuming to perform. It was concluded that the capacity of the FENTAB analysis went beyond the objectives of this thesis and was therefore abondon.

The modal analysis was a mode-superposition analysis of a distributed-parameter system and its solution was divided into its static and dynamic parts. More vibration modes were included in the modal analysis to represent the stresses with an acceptable degree of accuracy than were required to represent displacements. The modal analysi was a more direct and faster analysis which fulfilled the objectives of this thesis.

It is incorrect to rely on a specific value, such as the standard slow term failure

stress which is used in the traditional duration of loading theory.

The modal strength ratio was defined as the ratio between the dynamic failure stress and the static failure stress and was calculated from stress values from the modal analysis for each specimen. From the duration of load approach based on the modal strength ratio it was concluded that there was no difference in strength between the different static tests. The general tendency for the modal strength ratio approach was that the failure strength decreased with decreasing failure time for the impact tests. The modal strength ratio approach take the variation within the various loading groups into account because the modal strength ratio was computed directly for each specimen.

From the study of the strength ratio distribution it was concluded that the inertial velocity had an influence on the strength ratio for the strongest specimens among the intermediate and high drop-height tests.

The non-parametric 25th and 50th percentiles of the modal strength ratio formed on the basis of the ranked dynamic failure strength distribution were compared to the same percentiles formed on the basis of the ranked modal strength ratio distribution. The ranking of the modal strength ratio showed a more consistent tendency of decreasing strength with decreasing failure time as compared to the ranking of the dynamic failure stress. The modal strength artio appraoch offers a convenient and correct way to separate the dynamic effect of the loading type from the static strength of the specimen. It was concluded that during impact loading a strength decrease of 15 % could be expected for the weaker specimens compared to standard short term strength.

The failure modes were divided into compression initiated failure modes, brash initiated failure modes, and tension perpendicular to grain initiated failure modes. The brash initiated failure mode was a tension perpendicular to grain initiated failure

mode. The number of compression initiated failure modes decreased with decreasing failure times especially if the tension zone of the beam was strong. It was not possible to determine whether the tension perpendicular to grain failure mode was more dominating than the tension parallel to grain failure mode when the failure time decreased.

The decrease in failure strength with decreasing failure time was explained by the decreasing amount of compression initiated failure modes. Material with a strong tension zone developed more compression wrinkles in the compression zone, but as the failure time decreased the amount of failures in the tension zone increased and with that followed a decrease in failure strength.

Chapter 6

Conclusions

The behaviour of timber beams was studied under single blow impact. A better understanding and a more reliable quantification of the difference between static and impact loading was accomplished with this thesis.

1. From impact tests it was clear that the contact force between the impact loading head and the beam could be modelled as a ramp load.

2. The indentation and penetration problems from earlier impact tests were solved by placing a steel plate between the loading head and the specimen.

3. From damping tests the damping was considered to be negligible and therefore the dynamic system was assumed to be undamped.

4. From stress wave analysis the stress was considered to be transferred instantaneously throughout the beam for all the loading rates, because the stress travelled throughout the beam in less then 0.2 msec.

5. The failure load was determined as the maximum load experienced during a failure test.

6. In the earlier analysis it was assumed that the distribution of acceleration had the same distribution along the beam as the distribution of displacement. The large number of failures of measurements from the accelerometers raised serious concern about the reliability of the measurements from the accelerometers. The

main reason to abandon the earlier analysis was the unreliable measurements of the accelerometers.

7. The FENTAB analysis was the most flexible and detailed analysis. The capacity of the FENTAB analysis went beyond the objectives of this thesis and was therefore abandoned.

8. The modal analysis considers the energy input induced by the impact loading and the inertial forces occurring during impact loading.

9. The modal strength ratio was defined as the ratio between the dynamic failure stress and the static failure stress and was calculated for each specimen. The modal strength ratio approach offers a convenient and correct way to separate the dynamic effect of the loading type from the static strength of the specimen.

10. There were no difference in strength between different static tests. A strength decrease of 15 % could be expected during impact loading for the weaker specimen compared to the standard static strength of the specimen.

11. The decrease in failure strength with decreasing failure time for impact loading was explained by the decreasing number of compression initiated failure modes.

12. Material with a strong tension zone developed more compression wrinkles in the compression zone, but as the failure time decreased the number of failures in the tension zone increased and with that followed a decrease in failure strength.

Bibliography

ASTM (American Society of Testing Material), 1989.

1989 Annual book of ASTM standards Designation: D 198-84, Standard methods of static tests of timber in structural sizes. ASTM, Philadelphia, PA, USA.

Banthia, N.P., 1987.

Impact resistance of concrete. Ph.D. Thesis, Department of Civil Engineering, University of British Columbia, Vancouver, BC, Canada.

Bentur, A., Mindess, S. and Banthia, N., 1986.

The behavior of concrete under impact loading: Experimental procedures and method of analysis. Material and Structures (Materiaux et Constructions), Vol.19, No.113.

Bury, K.V., 1979.

Statistical analysis of NLGA tension tests. March 14.

Bury, K.V., 1986.

Statistical models in applied science. Robert E. Krieger Publishing Company, Malabar, Flo, USA.

Canadian Standard Association (CSA), 1989.

CAN/CSA-086.1-M89 Engineering design in wood (limit states design). CSA, Ottawa, Ont, Canada.

Clough, R.W. and Penzien, J., 1975.

Dynamics of structures. McGraw-Hill Inc, New York, NY, USA.

Drow, J.T., Markwardt, L.J. and Youngquist, W.G., 1958.

Results of impact tests to compare the pendulum impact and toughness test methods. U.S. Forest Service, Forest Products Laboratory, Report No.2109, Madison, Wi, USA.

Elmendorf, A., 1916.

Stresses in impact. Journal of the Franklin Institute, Vol. 182, No.6.

Folz, B.R., 1986.

Documentation for the program FENTAB (Finite Element Nonlinear Transient Analysis of Beams Version 1.0.) Department of Civil Engineering, University of British Columbia, Vancouver, BC, Canada, (Revised 1988).

Foschi, R.O., Folz, B.R. and Yao, F.Z., 1989.

Reliability-based design of wood structures. Structural Reseach Series, Report No. 34, Department of Civil Engineering, University of British Columbia, Vancouver, BC, Canada.

Harris, C.O., 1959.

Introduction to stress analysis. The MacMillan Company, New York, NY, USA.

Harris, C.M., 1988

Shock and vibration handbook. McGraw-Hill Book Company, New York, NY, USA.

Hoffmeyer, P., 1990.

Failure of wood as influenced by moisture and duration of load. Ph.D. Thesis, State University of New York, College of Enviromental Science and Forestry, Syracuse, NY, USA.

Ireland, D.R., 1974.

Procedures and problems associated with reliable control of the instrumented impact test. Instrumented Impact Testing, ASTM STP 563, American Society of Testing and Materials, pp. 3-29.

Kollmann, F.F.P. and Côté, W.A. Jr., 1968.

Principles of wood science and technology; part I: solid wood. Springer Verlag New York Inc, New York, NY, USA.

Liska, J.A., 1950.

Effect of rapid loading on the compressive and flexural strength of wood. U.S. Forest Service, Forest Products Laboratory, Report No. 1767, Madison, Wi, USA.

Lynn, P.A., 1989.

An introduction to the analysis and processing of signals. Macmillan Education Ltd, London, United Kingdom.

Madsen, B., 1971.

Duration of load tests for dry lumber in bending. Structural Research Series, Report No.3, Department of Civil Engineering, University of British Columbia, Vancouver, BC, Canada.

Madsen, B. and Buchanan, A.H., 1986.

Size effects in timber explained by a modified weakest link theory. Canadian Journal of Civil Engineering, Vol.13, No.2, pp. 218-232.

Madsen, B. and Mindess, S., 1986.

The influence of the energy stored in the test apparatus on the strength of lumber. Canadian Journal of Civil Engineering, Vol.13, No.1, pp.8-11.

Mindess, S. and Madsen, B., 1986.

The fracture of wood under impact loading. Material and Structures (Materiaux et Constructions), Vol.19, No.109, pp. 49-53.

Mindess, S., Madsen, B. and Yan, C., 1988.

Behaviour of timber beams under impact loading., Proceedings Colloque Scientifique Europeén: Comportement Mécanique du Bois, Bordeaux, France, pp.25-36.

Paz, M., 1985.

Structural dynamics. Van Nostrand Reinhold Company Inc, New York, NY, USA.

Pearson, E.S. and Harley, H.O., 1966.

Biometrika tables for statisticans. University Press, Cambridge, United Kingdom.

Somaskanthan, N., 1989.

Investigation of the dynamic fracture behavior of concrete. M.A.Sc. Thesis, Department of Civil Engineering, University of British Columbia, Vancouver, BC, Canada.

Spencer, R., 1978.

Rate of loading effect in bending for Douglas-fir lumber. Proceedings: 1st International Conference on Wood Fracture, Banff, Alb, Canada, pp. 259-279.

Wilson, T.R.C., 1922.

Impact tests of wood. Proceedings: American Society of Testing Materials, Vol.22, part II, pp. 55-73.

Wood, L.W., 1951.

Relation of strength of wood to duration of load. U.S. Forest Service, Forest Products Laboratory, Report No.1916, Madison, Wi, USA.

Zukas, J.A., Nicholas, T., Swift, H.F., Greszczuk, L.B. and Curran, D.R., 1982. **Impact dynamics.** John Wiley & Sons, Inc, New York, NY, USA.

Appendix A

Displacement Response

The displacement response expression is derived in this appendix at the midspan point ($x = L/2$) and at the failure time t_1. The simply supported beam is subjected to a ramp load, as defined in Equation 2.19, and an initial velocity at the mid-point. The homogenous solution of a generalized SDOF undamped system is accomplished by substituting the displacement expression of Equation 2.30 and the vibration shape expression given in the second equation of Equation 2.16 into the homogeneous solution of Equation 2.6 for an undamped SDOF system, and becomes

$$y_h(x,t) = \sum_n \sin\left(\frac{n\pi x}{L}\right)\left[A_n \cos(\omega_n t) + B_n \sin(\omega_n t)\right], \tag{A.1}$$

where n is number of modes, and A_n and B_n are constants.

The vibration shape expression given in the second equation of Equation 2.16 is also applicable for the partial solution expression of the undamped generalized SDOF system and is expressed as

$$y_p(x,t) = \sum_n \phi_n(x) Z_n(t). \tag{A.2}$$

If the vibration shape expression of the second equation of Equation 2.16 is substituted into in Equation 2.29 and A_1 is set equal to 1, then the expressions given for the generalized mass and the generalized load becomes

$$M_n = \frac{mL}{2} \quad \text{and} \quad P_n(t) = pt_1 \frac{t}{t_1} \sin\left(\frac{n\pi}{2}\right). \tag{A.3}$$

The time dependent term in the modal response expression of the particular solution, $Z_n(t)$, is solved by employing the Duhamel integral (Clough and Penzien, 1985; Paz, 1985) and gives

$$Z_n(t) = \frac{2pt_1 \sin\left(\frac{n\pi}{2}\right)}{mL\omega_n^2}\left(\frac{t}{t_1} - \frac{\sin(\omega_n t)}{\omega_n t_1}\right). \tag{A.4}$$

The total response for the generalized SDOF system is the sum of the homogeneous and the particular solution and becomes

$$y(x,t) = y_h(x,t) + y_p(x,t). \tag{A.5}$$

The constants A_n and B_n in the homogeneous expression are determined by substitution of the initial conditions into the total response expression. This results in

$$A_n = 0 \qquad \text{and} \tag{A.6}$$

$$B_n = \frac{2\dot{y}(0)}{\omega_n n\pi}(\cos(n\pi) - 1) \quad \text{at } x = L/2 \text{ otherwise } B_n = 0. \tag{A.7}$$

Finally the total displacement response at the mid-point ($x = L/2$) and at the failure time ($t = t_1$) becomes

$$y\left(\frac{L}{2}, t_1\right) = \sum_{n=1}^{\infty} \sin\left(\frac{n\pi}{2}\right)\left[\frac{2\dot{y}(0)}{\omega_n n\pi}(\cos(n\pi) - 1)\sin(\omega_n t_1) + \right.$$
$$\left. + \frac{2pt_1 \sin\left(\frac{n\pi}{2}\right)}{mL\omega_n^2}\left(1 - \frac{\sin(\omega_n t_1)}{\omega_n t_1}\right)\right]. \tag{A.8}$$

Appendix B

Strength Ratio

The strength ratio is defined as the ratio between the dynamic failure stress and the static failure stress. The failure is assumed to occur at the end of the pulse era at time t_1.

The failure stress expression of equation 2.33 for a ramp load is of the form

$$\sigma\left(\frac{L}{2}, t_1\right)\Big) = \frac{Ed\pi^2}{2L^2}\sum_{n=1}^{\infty} n^2 \sin\left(\frac{n\pi}{2}\right)\left[Y_n(t_1) + Z_n(t_1)\right], \tag{B.1}$$

at the mid-point ($x = L/2$) and at the failure time t_1. The failure stress expression for blast load and step load are of the same form as equation B.1. The terms within the square bracket are the only terms changing for the three impulsive loads. The same terms are also the only difference between dynamic failure stress and static failure stress for all three impulsive loads. At this stage the influence of initial velocity is neglected and therefore the term $Y_n(t_1)$ is set equal to zero. The strength ratio $R(t_1)$ becomes

$$R(t_1) = \frac{(Z_n(t_1))_{dynamic}}{(Z_n(t_1))_{static}}, \tag{B.2}$$

where $(Z_n(t_1))_{static}$ is

$$(Z_n(t_1))_{static} = \frac{F_n(t_1)}{K_n} = \frac{F_n(t_1)}{M_n\omega_n^2}, \tag{B.3}$$

where $F_n(t_1)$ is the generalized load and M_n is the generalized mass. For a static load this expression is the same for all the three impulsive loads, and therefore becomes

$$(Z_n(t_1))_{static} = \frac{2pt_1 \sin\left(\frac{n\pi}{2}\right)}{mL\omega_n^2}. \tag{B.4}$$

The strength ratio $R(t_1)$ is conveniently expressed in form of the impulsive length ratio (t_1/T) by substituting $\omega = 2\pi/T$. Finally the strength ratio $R(t_1/T)$ for the three impulsive load type at zero initial condition become:

$$\text{ramp:} \qquad R(t_1/T) = 1 - \frac{T}{2\pi t_1} \sin\left(\frac{2\pi t_1}{T}\right) \tag{B.5}$$

$$\text{blast:} \quad R(t_1/T) = \frac{T}{2\pi t_1} \sin\left(\frac{2\pi t_1}{T}\right) - \cos\left(\frac{2\pi t_1}{T}\right) \tag{B.6}$$

$$\text{step:} \qquad R(t_1/T) = 1 - \cos\left(\frac{2\pi t_1}{T}\right). \tag{B.7}$$

Appendix C

Experimental Aspects

Static Test Machine

This section contains some relevant data on the static test machine and a detailed description of the calibration of the static test set-up.

A test frame was used for mounting a MTS loading jack which was connected to a MTS control unit. A photograph and a schematic drawing are provided in Chapter 3.

- The hydraulic pump capacity was 22.7 dm^3/sec (5 imperial gallon/min).
- The MTS hydraulic actuator (model 204.61, serial no. 333) had a force capacity of $\pm$ 76 MPa (11 kips), a maximum stroke length of 25.4 mm (10 in) and a actuator area of 2420 mm^2 (3.75 in^2).
- The maximum theoretical load capacity was approximately 180 kN.
- The actuator could theoretically be moved with an approximate maximum velocity of 157 mm/sec (4.9 in/sec).
- The loadcell had a load capacity of 49 kN (5 metric tons).

Calibration of Static Test Machine

The actuator and loadcell of the MTS machine were both calibrated. The tup of the loadcell measured the load. The position of the actuator was given in volts. The loadcell was calibrated against the loading scale of the test frame machine which measured the load in pounds. A solid block of wood was loaded in compression at approximately the same position the beam specimen later would be tested. Load readings were compared with the voltage output from the Notebook software. The voltage span in the MTS set-up was ± 10 volts. Measurements were taken at each volt up to 8 volts load. The load at 8 volts was almost 30 kN, which was higher than the expected maximum failure load.

The voltage measurement from the actuator was calibrated against an ordinary dial gauge located where the beam specimen later would be tested. Measurements were taken for each 0.1 in up to 0.9 in deflection. One displacement calibration was performed for the modulus of elasicity tests and another for the static tests. For the modulus of elasticity tests calibration the maximum deflection was estimated to 0.9 in (22.9 mm). After a few preliminary failure tests this maximum deflection was found to be not sufficient. Therefore a new calibration was conducted for the static tests.

Linear regression analysis was carried out by using 1-2-3, a program software from Lotus Development Corparation, Cambridge, Mass., USA. The intercept was set at the origin. Table C.1 show the calculated calibration factor and in the brackets its standard error.

Table C.1: Calibration factors.

calibration factor	displacement mm/volt	load kN/volt
MOE-tests	1.816(0.002)	3.585(0.012)
static-tests	3.730(0.006)	3.585(0.012)

Impact Test Machine

This section includes some relevent data on the impact loadcell and the accelerometers used for some of the impact tests together with a detailed description of the calibration procedure for the impact test machine.

The impact test machine used was an instrumented drop-weight (the French guillotine) impact machine. A photograph and a schematic drawing are provided in Chapter 3.

- The loadcell had a maximum load capacity of 134 kN.
- The resolution of the accelerometer was 0.01 g.
- The resonant frequency for the accelerometer was 45 kHz.
- The maximum vibration/shock for the accelerometer was 5000 g.
- The load recovery for the accelerometer was less then 10μ seconds.
- The sensitivity of the accelerometer was 10 mV/g (± 0.2).

Calibration of Impact Test Machine

A static calibration was performed by loading and unloading the impact tup essembly in an Instron Universal Testing Instrument machine (model 4206) in the Material Testing Laboratory at the Department of Civil Engineering (UBC). Voltage was read with a voltmeter, Fluke 8050A Digital Multimeter, at a certain load levels. The loadlevels were read on the digital display of the Instron machine on the output line of the data aquisition system.

Power supply came from the same data aquisition system, which was used during the impact testing, and no analog filters were applied. The tests were performed up

to 30 kN with the crosshead speed of 1.0 mm/min with voltage reading every 2 kN on both the loading and unloading path. The voltage gain of the data aquisition system changed the voltage output from milli-volts to volts and was set once and for all for the loadcell channel.

The linear regression analysis was performed by Lotus 1-2-3 in which the intercept between voltage and load was set equal to zero. Two identical calibration tests were performed. They gave a calibration factors of 5.867 kN/V and 5.849 kN/V. The power for the system is shut off for 2 hours and immidiatly thereafter two more calibration tests were performed which gave calibration factors of 5.778 kN/V and 5.772 kN/V. In order, in some way, to simulate a relocation of the data aquisition system from the Material Testing Laboratory to the Structural Laboratory the power was again shut off and the data aquisition system was carefully moved around for 5 minutes. After another 5 minutes stabilization two more tests were performed which gave calibration factors of 5.758 kN/V and 5.756 kN/V. It was concluded that the data aquisition system was reasonably stable even after the relocation as long as the system was given some time to stabilize. Linear regression analysis was conducted on all of the last six calibration tests (approximately 220 data points) and the calibration factor was found to be 5.796 kN/V with a 0.004 kN/V standard error. The same path was followed for loading and unloading in all the calibration tests.

Sampling Rates

A reasonable accuracy of testing results was assumed to be accomplished if an estimated 64 ($= 2^6$) points per measurement were collected during each static loading event. The sampling increment (Δt) is equal to $\Delta t = T/N$, where T is the expected failure time or interesting time record and N is the number of point per measurement. The lowest frequency component (Δf) is measureable from a time record as

Table C.2: Sampling rates for static tests.

loading rates	T sec	Δf Hz	Δt msec	f_s Hz
slow	60	0.0167	937.5	1.067
intermediate	3.5	0.2857	54.7	18.286
fast	0.2	5.0000	3.1	320.000

$1/T$. The sampling frequency or sampling rate f_S is then $1/\Delta t$.

Table C.2 shows the failure times, lowest frequency component, sampling increments, and sampling rates for the static tests.

Specimen

The following defects were given special attention and led to four different timber sub-groups:

- a centrally ($\pm$ 25 mm) located large ($>$ 10 mm) wide bottom faced or narrow faced knot
- more then one large ($>$ 10 mm) knots in the lower portion of middle 1/2 span
- centrally located ($\pm$ 25 mm) indication of slope of grain failure at the bottom edge
- another indication of weakness in the lower portion of middle 1/2 span

The areas associated with the central ($\pm$ 25 mm) and lower portion of middle 1/2 span are hatched in Figure C.1.

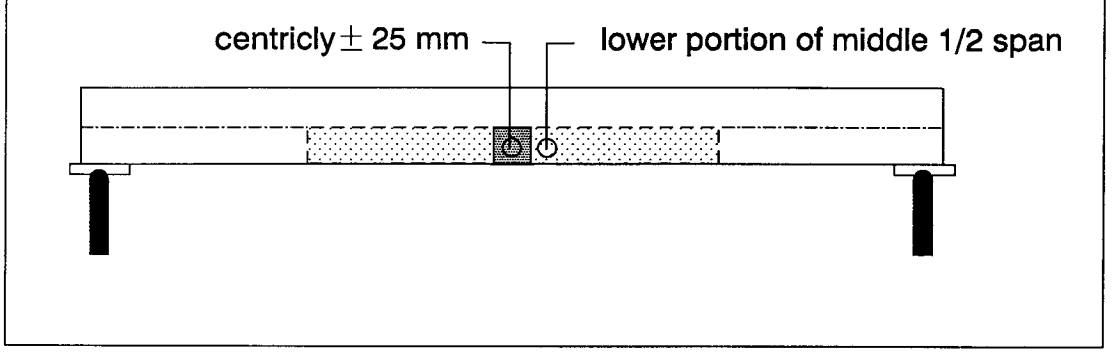

Figure C.1: Hatched areas of specimen.

Sample Sizes

An estimate of required sample sizes was obtained from the two-sided test on the expected value for a normal distribution (Bury, 1989). A confidence of 95% and a power of 95% are assigned for this test. The confidence is related to the "consumer risk" α or the acceptance of an unadequate product. The power is related to the "producer risk" β or the rejection of an adequate product. Both these risks are set to 5%. A two-sided test means that it is not known whether the estimate is larger or smaller than the underlying quantity. The required sample size n is

$$n \geq \left(\frac{z_{(1-\alpha/2)} - z_{\beta}}{\Delta\mu} \right)^2 \sigma^2 \tag{C.1}$$

where $z_{(1-\alpha/2)}$ and z_{β} are the standard normal quantiles of order $(1-\alpha/2)$ respective β.

The z-values are 1.96 and 1.645 respectively (Pearson and Hartley, 1966). In another investigation the 2-parameter Weibull distribution was fitted to the distribution of modulus of rupture from Canadian Wood Counsil's (CWC) in-grade testing

program (Foschi et al., 1989). For 38 x 89 mm Select Structural (SS) of the spruce-pine-fir (SPF) the mean value μ was 52.46 MPa and the coefficient of variation was 0.21. The standard deviation σ became 11.02 MPa.

The $\Delta\mu$ value is the location shift of the average value that can be detected and is set equal to 5 MPa. The sample size demanded with these risks was more than 63 specimen.

Appendix D

MathCAD Calculation

This appendix contains a copy of the output from one of the MathCAD calculations performed on one of the loading rates.

ORIGIN := 1 SDC8H2

STRENGTH DISTRIBUTION from a MODAL close form solution and STRENGTH RATIO for failure (t=tI) of C8H2 at x=L/2 with 47 terms

Input: $D := READPRN(DATA)$

Beams: $i := 1..58 \quad L := 1095 \cdot mm \quad \rho := 480 \cdot kg \cdot m^{-3}$

$b_i := D_{i,1} \cdot mm \quad d_i := D_{i,2} \cdot mm \quad E_i := D_{i,3} \cdot MPa \quad I_i := \frac{b_i \cdot d_i^3}{12}$

$md_i := \rho \cdot b_i \cdot d_i$

Loading: $tI_i := D_{i,4} \cdot sec \quad ptI_i := D_{i,5} \cdot kN \quad v0 := 1.6 \cdot \frac{m}{sec}$

Shape function: $M := 24 \quad j := 1..M \quad n_j := 2 \cdot j - 1 \quad n_M =$

$\phi_j := \sin\left[\frac{n_j \cdot \pi}{2}\right]$

Eigenvalue: $\omega_{i,j} := [n_j \cdot \pi]^2 \cdot \sqrt{\frac{E_i \cdot I_i}{md_i \cdot L^4}} \quad \omega 1_i := \omega_{i,1} \quad f1_i := \frac{\omega 1_i}{2 \cdot \pi} \quad T1_i := \frac{1}{f1_i}$

$O_{i,1} := \omega 1_i \cdot \frac{sec}{rad} \quad O_{i,2} := f1_i \cdot \frac{1}{Hz} \quad O_{i,3} := T1_i \cdot \frac{1}{msec}$

Displacement: $Y_{i,j} := \frac{2 \cdot v0 \cdot [\cos[n_j \cdot \pi] - 1] \cdot \sin[\omega_{i,j} \cdot tI_i]}{\omega_{i,j} \cdot n_j \cdot \pi}$

Units: $m \equiv 1L \quad kg \equiv 1M \quad sec \equiv 1T \quad rad \equiv 1 \quad mm \equiv 0.001 \cdot m \quad msec \equiv 0.001 \cdot sec$

$Hz \equiv sec^{-1} \quad N \equiv kg \cdot m \cdot sec^{-2} \quad Pa \equiv N \cdot m^{-2} \quad MPa \equiv 10^6 \cdot Pa$

$kN \equiv 1000 \cdot N \quad kNm \equiv kN \cdot m \quad kHz \equiv 1000 \cdot Hz$

$$Zst_{i,j} := \frac{2 \cdot ptI_i \cdot \sin\left[\frac{n_j \cdot \pi}{2}\right]}{md_i \cdot L \cdot \omega_{i,j}^2}$$

$$Z_{i,j} := Zst_{i,j} \cdot \left[1 - \frac{\sin[\omega_{i,j} \cdot tI_i]}{\omega_{i,j} \cdot tI_i}\right]$$

$$yst_{i,j} := \phi_j \cdot Zst_{i,j} \qquad y_{i,j} := \phi_j \cdot [Y_{i,j} + Z_{i,j}]$$

$$ystmax_i := \sum_j yst_{i,j} \qquad ymax_i := \sum_j y_{i,j}$$

$$O_{i,4} := ystmax_i \cdot \frac{1}{mm} \qquad O_{i,5} := ymax_i \cdot \frac{1}{mm}$$

Stress:

$$\sigma st_{i,j} := \left[\frac{E_i \cdot d_i^2 \cdot \pi^2}{2 \cdot L^2}\right] \cdot [n_j^2 \cdot \phi_j \cdot Zst_{i,j}] \qquad \sigma stmax_i := \sum_j \sigma st_{i,j}$$

$$\sigma_{i,j} := \left[\frac{E_i \cdot d_i^2 \cdot \pi^2}{2 \cdot L^2}\right] \cdot [n_j^2 \cdot \phi_j \cdot [Y_{i,j} + Z_{i,j}]] \qquad \sigma max_i := \sum_j \sigma_{i,j}$$

$$O_{i,6} := \sigma stmax_i \cdot \frac{1}{MPa} \qquad O_{i,7} := \sigma max_i \cdot \frac{1}{MPa}$$

SR ratio:

$$yRR_i := \frac{ymax_i}{ystmax_i} \qquad \sigma SR_i := \frac{\sigma max_i}{\sigma stmax_i} \qquad O_{i,8} := yRR_i \qquad O_{i,9} := \sigma SR_i$$

Output:

WRITEPRN(OUT) := O